Biophysical *Journal*

Volume 113 Number 8 Pages 000–000 October 17, 2017

Biophysical *Journal*

The Premier Journal of Quantitative Biology

Volume113
Number 8
October 17, 2017

www.biophysj.org

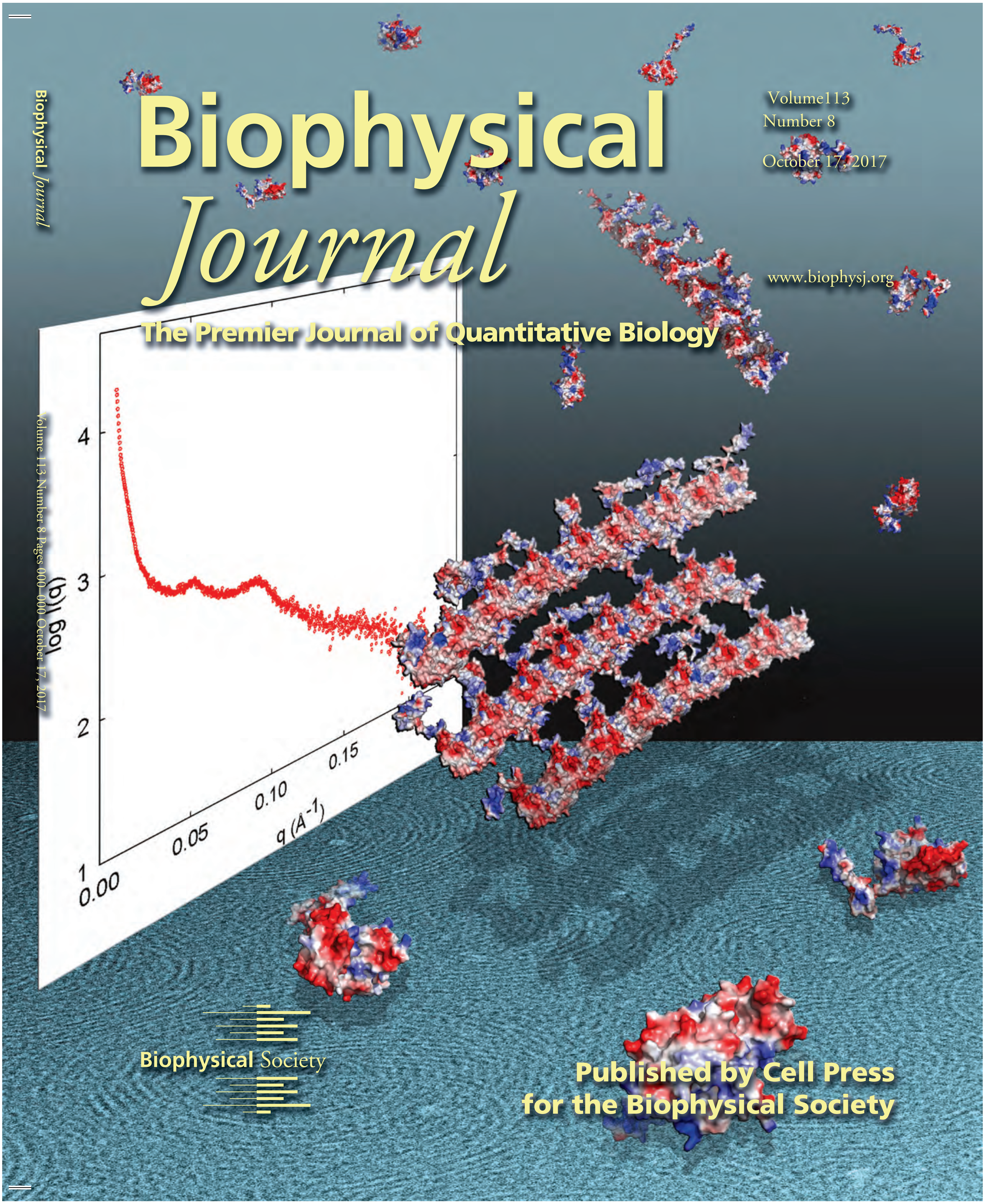

Biophysical Society

Published by Cell Press
for the Biophysical Society

Biophysical *Journal*
Article

Biophysical Society

Self-Organization of FtsZ Polymers in Solution Reveals Spacer Role of the Disordered C-Terminal Tail

Sonia Huecas,[1] Erney Ramírez-Aportela,[2] Albert Vergoñós,[1] Rafael Núñez-Ramírez,[1] Oscar Llorca,[1,3] J. Fernando Díaz,[1] David Juan-Rodríguez,[1] María A. Oliva,[1] Patricia Castellen,[1,4] and José M. Andreu[1,*]
[1]Centro de Investigaciones Biológicas and [2]Instituto de Quimica Fisica Rocasolano, CSIC, Madrid, Spain; [3]Spanish National Cancer Research Center, CNIO, Madrid, Spain; and [4]Department of Chemistry, State University of Ponta Grossa, Paraná, Brazil

ABSTRACT FtsZ is a self-assembling GTPase that forms, below the inner membrane, the mid-cell Z-ring guiding bacterial division. FtsZ monomers polymerize head to tail forming tubulin-like dynamic protofilaments, whose organization in the Z-ring is an unresolved problem. Rather than forming a well-defined structure, FtsZ protofilaments laterally associate in vitro into polymorphic condensates typically imaged on surfaces. We describe here nanoscale self-organizing properties of FtsZ assemblies in solution that underlie Z-ring assembly, employing time-resolved x-ray scattering and cryo-electron microscopy. We find that FtsZ forms bundles made of loosely bound filaments of variable length and curvature. Individual FtsZ protofilaments further bend upon nucleotide hydrolysis, highlighted by the observation of some large circular structures with 2.5–5° curvature angles between subunits, followed by disassembly end-products consisting of highly curved oligomers and 16-subunit −220 Å diameter mini-rings, here observed by cryo-electron microscopy. Neighbor FtsZ filaments in bundles are laterally spaced 70 Å, leaving a gap in between. In contrast, close contact between filament core structures (~50 Å spacing) is observed in straight polymers of FtsZ constructs lacking the C-terminal tail, which is known to provide a flexible tether essential for FtsZ functions in cell division. Changing the length of the intrinsically disordered C-tail linker modifies the interfilament spacing. We propose that the linker prevents dynamic FtsZ protofilaments in bundles from sticking to one another, holding them apart at a distance similar to the lateral spacing observed by electron cryotomography in several bacteria and liposomes. According to this model, weak interactions between curved polar FtsZ protofilaments through their the C-tails may facilitate the coherent treadmilling dynamics of membrane-associated FtsZ bundles in reconstituted systems, as well as the recently discovered movement of FtsZ clusters around bacterial Z-rings that is powered by GTP hydrolysis and guides correct septal cell wall synthesis and cell division.

INTRODUCTION

FtsZ is a tubulin-like polymerizing GTPase that directs the cell division machinery in most bacteria. FtsZ forms the mid-cell Z-ring (1), which is attached to the inner side of the plasma membrane by tethering proteins including the conserved actinlike FtsA. The Z-ring serves as a dynamic scaffold that recruits the other divisomal proteins, including cell wall synthesis and remodeling enzymes, and regulates peptidoglycan metabolism. The Z-ring constricts during cell division and contractile FtsZ rings have been reconstituted on liposomes. However, more substantial constriction force appears to be provided by septal peptidoglycan synthesis in *Escherichia coli*, where the divisome is a multilayered protein network, and FtsZ disassembles from the division site before compartmentalization (2–5).

The nanoscale organization of the Z-ring in different bacteria has been studied with superresolution (SR) microscopy methods (6–13) and with polarized fluorescence microscopy (14) employing FtsZ-fluorescent protein fusions. These studies support a discontinuous Z-ring made of loosely associated, disordered FtsZ clusters. On the other hand, electron cryotomography studies have identified a few FtsZ filaments (15) or a continuous small band of filaments one-FtsZ-molecule wide (16) that are 150 ± 20 Å below the plasma membrane. FtsZ filaments were 93 Å (15) or 78 Å (16) apart from each other (center to center distance) in *Caulobacter crescentus* (Cc) and at 68 Å in *E. coli* (Ec) cells. Filaments were laterally spaced 78 Å, on average, in reconstituted rings made of *Thermotoga maritima* (Tm) FtsZ and FtsA in liposomes (16).

Submitted March 14, 2017, and accepted for publication August 30, 2017.

*Correspondence: j.m.andreu@cib.csic.es

Sonia Huecas and Erney Ramírez-Aportela contributed equally to this work.

Editor: David Sept.
http://dx.doi.org/10.1016/j.bpj.2017.08.046

Circular assemblies of FtsZ filaments flexibly attached to model membranes have been observed in several in vitro reconstituted systems. Contractile rings in liposomes (17,18) and protofilament ribbons on membrane tubules (19) were assembled from EcFtsZ fused with a fluorescent protein and a membrane-targeting sequence (FtsZ-Mts). Polymers of FtsZ-Mts were preferentially oriented at angles dependent on the curvature of supported membranes (20). TmFtsZ and TmFtsA filaments formed spirals, continuous rings, and domes inside liposomes, and the rings in liposome constrictions were 300–900 Å in diameter; this electron cryo-tomography study (16) favored a mechanism for membrane constriction involving FtsZ filament condensation and sliding (21). Strikingly, EcFtsZ filaments attached via EcFtsA to flat membranes at a high-protein density, self-organized, forming directionally moving bundles and ~1.2-μm-diameter vortices that exhibited chiral rotation. Single filaments were observed at low protein density. Filament head-to-tail polymerization (treadmilling) and fragmentation, but no sliding, was observed in these experiments in which single FtsZ molecules were stationary (22), supporting an FtsZ polymer recycling mechanism for Z-ring constriction (15). It has been recently shown that FtsZ-Mts can also form 1 μm chiral vortices powered by GTP without FtsA, indicating that the dynamic self-organization observed is an intrinsic property of FtsZ polymers when supplemented with a reversible membrane anchor (23).

Numerous physical models for the Z-ring have been proposed in which opposing mechanisms were considered, such as constriction involving filament bending upon GTP hydrolysis, or filament sliding or filament recycling dynamics (24). Highly curved FtsZ filaments were observed to form negatively stained mini-rings made of 16 subunits, but an intermediately curved conformation was hypothesized to generate constriction force (25). However, most microscopy images of FtsZ circular assemblies were previously obtained from FtsZ adsorbed to lipid, carbon, or mica surfaces, which may modify the filaments curvature with respect to FtsZ filaments in solution or flexibly attached to a membrane.

The FtsZ structure consists of two tubulin-like (N-terminal) GTP-binding and GTPase-activating domains (26) followed by a flexible C-terminal region of variable length depending on the bacterial species. FtsZ monomers assemble head to tail forming single-stranded protofilaments, in which the GTPase site is completed at a tight subunit-subunit interface, represented by the crystal structure of *Staphylococcus aureus* (Sa) FtsZ filaments (27,28). The GTP γ-phosphate and a coordinated Mg^{2+} ions are key to holding this longitudinal interface closed (29). GTP hydrolysis to GDP loosens the FtsZ-FtsZ interface, possibly by a hinge-opening mechanism (29,30) and triggers disassembly, which can be followed by monomers spontaneously reloading with GTP. The monomers association is allosterically coupled to a structural change within each monomer. Thus, single-stranded FtsZ filaments assemble cooperatively, involving monomers switching between low- and high-association affinity conformations (31), in which the side cleft between the protein domains is respectively closed or open (27,29,32,33). This structural switch explains treadmilling dynamics of FtsZ filaments (33). The antibacterial inhibitor PC190723 (34) stabilizes FtsZ filaments (35) by binding into the open cleft (27).

The flexible C-terminal tail, which is missing from FtsZ crystal structures, is essential for FtsZ function. It consists of a C-terminal linker (CTL) of variable length followed by an 11-residue conserved sequence (CTC) and short C-terminal variable sequences (CTV). The FtsZ CTC sequence is essential for membrane tethering through FtsA and ZipA and it is also a hub for interaction with modulatory proteins (36). The six-residue basic CTV end of *Bacillus subtilis* FtsZ (BsFtsZ) ensures efficient division and mediates lateral electrostatic interactions between filaments in bundles, whereas the four-residue EcFtsZ CTV does not promote bundling (36). The intrinsically disordered CTL linker is a nonconserved peptide of quite variable length that functions as a flexible tether between FtsZ filaments for proper assembly, for interaction with cytoplasmic modulatory proteins, and for membrane attachment (37), thus playing a critical role in bacterial division (38). Moreover, the CTL is required to guide robust cell wall cross-linking during division of *C. crescentus* (39).

We have analyzed the low-resolution structures of FtsZ polymers in solution, employing time-resolved small angle x-ray scattering (SAXS), molecular models, and cryo-electron microscopy (cryo-EM); we used FtsZs from different organisms under varying solution conditions. We have found that 1) FtsZ forms loose bundles of protofilaments of variable length and intrinsic curvature in solution, 2) the disordered C-terminal tail provides a flexible ~70 Å spacer between FtsZ protofilaments in bundles, and 3) FtsZ protofilaments bend upon GTP hydrolysis in solution and form rings without requiring a support. These results provide insight into the self-organizing properties of FtsZ assemblies relevant for the organization and dynamics of the Z-ring.

MATERIALS AND METHODS

FtsZ proteins and constructs (Table S1), purification, polymerization, biochemical methods, SAXS experiments, FtsZ single filaments and bundle SAXS models, and cryo-EM, are described in the Supporting Material. Experimental conditions are as follows: BsFtsZ was assembled in 50 mM Tris-HCl, 50 mM KCl, 1 mM EDTA pH 7.4, 25°C (Tris 50 buffer), with 10 mM $MgCl_2$ and 0.1 mM GMPCPP or 1 mM GTP. EcFtsZ assembly was in 25 mM PIPES/KOH, 250 mM KCl, 1 mM EDTA, pH 7.5, 25°C (PIPES 250 buffer), or in Tris 50 buffer for comparison, with 10 mM $MgCl_2$ and 0.1 mM GMPCPP or 1 mM GTP, or a GTP regenerating system. FtsZ from *Methanocaldococcus jannaschii* (MjFtsZ) assembled in 50 mM Mes/KOH, 50 mM KCl, 1 mM EDTA, pH 6.5, 55°C (Mes50 buffer) with 10 mM $MgCl_2$ and 0.2 mM GMPCPP or 4 mM GTP.

RESULTS

X-ray solution scattering by BsFtsZ monomers

We first analyzed SAXS by BsFtsZ subunits as a reference state for FtsZ polymers. BsFtsZ remains monomeric at relatively high concentrations in the absence of magnesium (40), unlike oligomer forming EcFtsZ (41) and MjFtsZ (42). BsFtsZ behaved as a nonisometric particle with radius of gyration $R_G = 32.1 \pm 1.0$ Å and a maximal dimension $D_{\max} \sim 120$ Å (Fig. 1 *A*, *solid circles* and *lines*). These values are larger than calculated from the crystal structure of the BsFtsZ globular core (Fig. 1 *A*, *inset*), which lacks the first 11 N-terminal and last 67 C-terminal residues, including the 51-residue intrinsically disordered linker (36,37). An R_G value of ~20 Å would be predicted for the linker itself (43). Therefore, we mainly attributed the excess scattering dimensions of BsFtsZ over the core crystal structure to the disordered C-terminal tail. This was supported by SAXS measurements of tag-BsFtsZ-ΔCt, a construct lacking the 67-residue C-terminal tail (GSHMAS-BsFtsZ (1–315), with the 6 N-terminal extra residues remaining from the affinity tag; Fig. 1 *A*, *shaded circles* and *lines*), which gave reduced values of $R_G = 24.9 \pm 1.3$ Å and $D_{\max} \sim 85$ Å. Sedimentation velocity analysis under identical solution conditions indicated hydrodynamic particles with similar $s_{20,w}$ values, 3.0 S (tag-BsFtsZ-ΔCt) and 3.2 S (BsFtsZ) corresponding to FtsZ monomers (40,41), in which the excess mass of the full-length protein is in good part compensated by the increased friction of the disordered C-tail (Fig. 1 *B*).

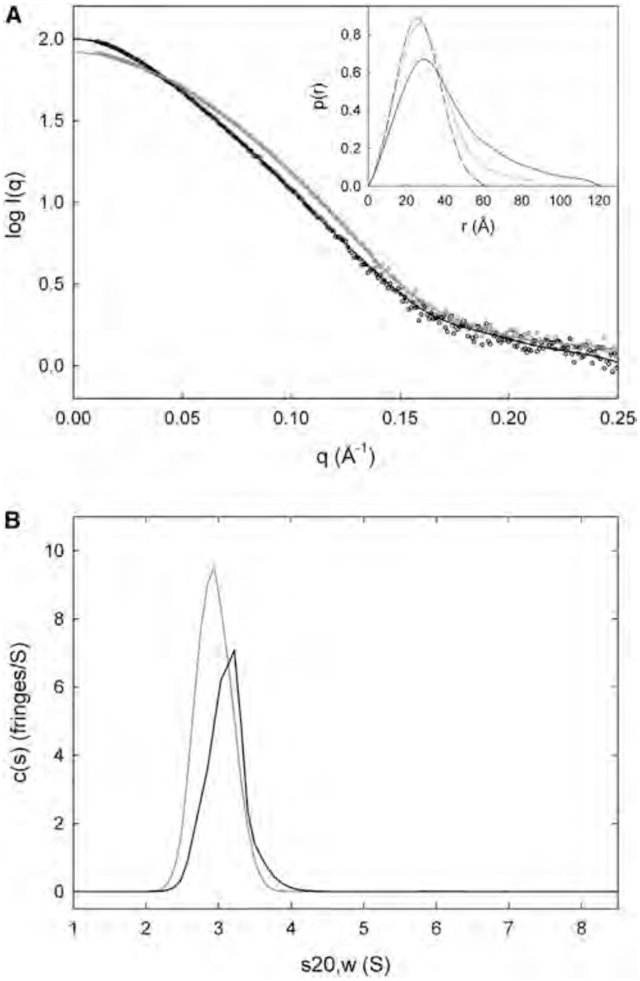

FIGURE 1 SAXS by monomers of full-length and truncated BsFtsZ. (*A*) Given here are SAXS profiles of 50 μM BsFtsZ (*solid circles*) and BsFtsZ-ΔCt lacking the disordered C-terminal tail (*shaded circles*), in Tris 50 buffer with 1 mM GDP at 25°C. The lines are the respective regularized GNOM fits. The R_G values were: BsFtsZ, 32.5 ± 0.5 Å (GNOM) and 31.8 ± 1.3 Å (Guinier plot); tag-BsFtsZ-ΔCt, 25.1 ± 0.1 Å (GNOM) and 24.7 ± 1.8 Å (Guinier). The inset shows the pair distribution functions of BsFtsZ (*solid line*), tag-BsFtsZΔCt (*shaded line*), and the theoretical curve calculated from the crystal structure of BsFtsZ lacking the first 11 and last 67 residues (*dashed line*; PDB: 2VXY; $R_G = 20.5$ Å, $D_{\max} = 60$ Å). (*B*) Given here are sedimentation coefficient distributions of BsFtsZ (*solid line*) and tag-BsFtsZ-ΔCt (*shaded line*) under identical conditions to SAXS determined by analytical ultracentrifugation and SEDFIT processing (see Materials and Methods). BsFtsZ: $s_{20,w} = 3.2$ S, estimated $f/f_{\min} = 1.4$, $Mr \sim 44{,}600$ (theoretical, 40,400) from the SEDFIT sedimentation-diffusion analysis. tag-BsFtsZ-ΔCt: $s_{20,w} = 3.0$ S, estimated $f/f_{\min} = 1.3$, $Mr \sim 37{,}700$ (theoretical, 33,200).

Time-resolved x-ray scattering by BsFtsZ polymers

We measured time-resolved SAXS by steady state and disassembling BsFtsZ polymers, to determine their collective structural features. BsFtsZ monomers assemble into filamentous polymers upon addition of magnesium and guanosine triphosphate nucleotide, which is then hydrolyzed; this is followed by polymer disassembly upon nucleotide consumption (35). BsFtsZ (50 μM) assembled with GTP has a steep lower angle scattering zone ($q = 0.01$ to ~ 0.02 Å^{-1}; central scattering), indicative of large polymers, and a maximum at $q = 0.09$ Å^{-1}, corresponding to a distance $d = 70$ Å in real space ($d = 2\pi/q$), hypothetically arising from the lateral spacing between neighbor protofilaments in polymers (Fig. 2 *A*). We were initially surprised by the smooth scattering profile above 0.10 Å^{-1}, lacking a clear maximum at $q = 0.14$ Å^{-1}, which we expected from the 44 Å spacing of monomers along FtsZ protofilaments (27,35,44). In comparison, steady-state BsFtsZ polymers assembled with the slowly hydrolysable analog GMPCPP have a more marked 0.09 Å^{-1} maximum and an additional low angle maximum at 0.05 Å^{-1}, corresponding to a spacing of 126 Å (Fig. 2 *A*, *red points*). The central scattering by BsFtsZ-GMPCPP polymers was steeper than with GTP, indicating quite large scattering objects. These samples were visually turbid when loaded into the SAXS cell and turned transparent upon nucleotide consumption and disassembly during measurements, whereas the GTP samples were mostly clear. This indicated for the BsFtsZ-GMPCPP polymers a size larger than the visible light wavelength,

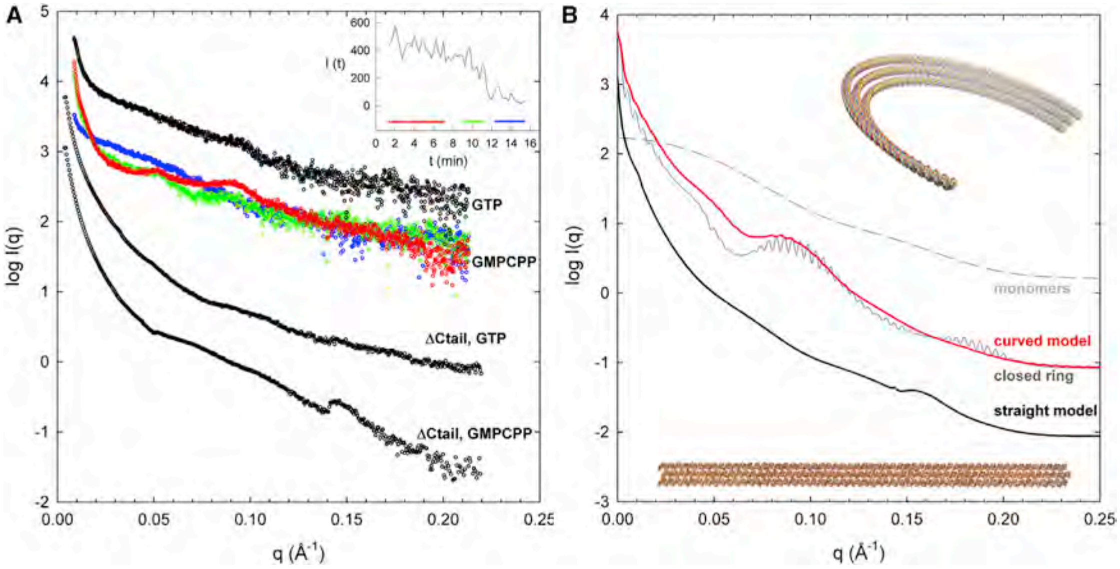

FIGURE 2 Time-resolved SAXS by full-length BsFtsZ, C-terminal truncated BsFtsZ, and computed SAXS profiles of selected FtsZ polymer models. (*A*) Polymers were assembled from BsFtsZ (50 μM) in Tris 50 buffer with 10 mM $MgCl_2$ and 1 mM GTP (*black profile on top*, initial time frames) or 0.1 mM GMPCPP (*superposed color profiles*) at 25°C. The red profile is an average measurement of the initial polymers, the green profile during depolymerization upon GMPCPP hydrolysis, and the blue profile after depolymerization. The degree of polymerization was monitored by the central x-ray scattering along the experiment in 15-s time frames (*inset*, where the zones averaged are indicated) and in preparatory off-line light scattering tests. The two lower profiles (in *black*) are the scattering by polymers of truncated tag-BsFtsZ-ΔCt, with GTP and GMPCPP. The profiles are vertically shifted to facilitate comparisons. (*B*) FtsZ polymer models were constructed based on the crystal filaments of homologous SaFtsZ and their solution scattering profiles were calculated (see main text and Materials and Methods). Two polymer models among many others (Figs S2, S3, S4, and S5) are shown: one consists of three straight protofilaments, each made of 60 monomers laterally spaced 48 Å center to center (*bottom*, *black scattering curve*). The other is a loose bundle made of three equivalent curved filaments laterally spaced 70 Å, with a mean curvature angle of 3.4° per monomer (*top* and *red scattering curve*; this model contains 40,400 atoms and its end-to-end distance is 1400 Å). The scattering profile corresponding to a triple ring obtained by circularly closing the curved model is also shown (*gray line*). The computed x-ray scattering curves (Figs. S3 and S4) have been combined in each case with a 5% of unassembled BsFtsZ monomers to generate the profiles shown here. The scattering by BsFtsZ monomers is indicated by the dashed line, which is the regularized scattering profile of BsFtsZ (Fig. 1 *A*), scaled to the theoretical scattering profile of 180 SaFtsZ model monomers at zero angle. The model SAXS profiles should be qualitatively compared with the experimental profiles in (*A*). To see this figure in color, go online.

precluding measurement of their longitudinal dimensions (R_G, $D_{\max}$) with our x-ray scattering setting ($q_{\min}$ = 0.01 Å^{-1}). BsFtsZ polymers disassembly could be monitored by the decrease in central scattering (Fig. 2 *A*, *inset*), which was accompanied by the progressive disappearance of the 0.05 and 0.09 Å^{-1} maxima. No other scattering features were observed that would support the formation of different intermediate polymer species during disassembly, in sufficient abundance to be detected, except for FtsZ oligomers indicated by the residual lower angle scattering after disassembly (Fig. 2 *A*, *green points*, mid-disassembly; *blue points*, end-state. One sample with GDP gave a profile similar to the end-state).

We examined the effects on SAXS of ligands that induce or inhibit BsFtsZ assembly. The FtsZ polymer-stabilizing compound PC190723 enhanced and slightly shifted the BsFtsZ-GMPCPP polymer 0.05 and 0.10 Å^{-1} scattering maxima; it also enhanced the central scattering, the 0.08 Å^{-1} maximum in BsFtsZ-GTP polymers (Fig. S1), and inhibited depolymerization; these observations are compatible with the expected formation of PC190723-induced filament bundles (35). When PC190723 was added to BsFtsZ-GMPCPP in the absence of Mg^{2+}, it only enhanced the central scattering, as expected from the ligand-induced formation of single protofilaments (35). On the other hand, adding the assembly inhibitor UCM53 (45) to BsFtsZ-GTP polymers decreased the central scattering, indicating a reduction in the degree of polymerization (Fig. S1). These results supported our SAXS analysis of FtsZ assembly.

Distinct x-ray scattering by polymers of a BsFtsZ construct lacking the C-terminal tail

We observed in light scattering tests that tag-BsFtsZ-ΔCt assembled better, had lower critical protein concentration (Cr) for assembly, and its polymers lasted for longer than those of native BsFtsZ, whereas full-length tag-BsFtsZ (GSHMAS-BsFtsZ) assembled similarly to BsFtsZ (Materials and Methods). Tag-BsFtsZ-ΔCt polymers had reduced GTPase activity. The GTP (2 mM) hydrolysis rates were: BsFtsZ 1.12 ± 0.09, tag-BsFtsZ-ΔCt 0.62 ± 0.08, tag-BsFtsZ 0.95 ± 0.05 min^{-1}; the corresponding rates of hydrolysis of GMPCPP (0.1 mM) were 0.19 ± 0.02, 0.032 ± 0.003 and 0.27 ± 0.02 min^{-1}, respectively. We determined the SAXS profile of tag-BsFtsZ-ΔCt polymers, which showed several striking differences with respect to the full-length protein. The 0.09 and 0.05 $Å^{-1}$ maxima, which we had attributed to 70 and 126 Å lateral spacings between BsFtsZ protofilaments, were absent in the tag-BsFtsZ-ΔCt polymers (Fig. 2 *A*). This indicated different lateral interactions in the tail-less FtsZ protofilaments (analyzed below). In addition, a marked bulge-shape maximum was observed at 0.143 $Å^{-1}$ with GMPCPP, as would be expected from the 44 Å axial spacing between subunits in FtsZ protofilaments.

Model analysis of x-ray scattering by BsFtsZ and tail-less filament bundles

To gain further insight into the solution structure of FtsZ polymers, we constructed a comprehensive series of models based on the filament crystal structure of SaFtsZ, seeking to reproduce the experimental SAXS features of FtsZ polymers, without any other initial information. SaFtsZ is a close homolog of BsFtsZ, and the crystal structures of FtsZ monomers from different species are all very similar (33). Notice that at our ~30 Å experimental resolution the more prominent model scattering features are dominated by the arrangement of subunits rather than by their internal structure. The disordered C-terminal extension (spanning 75-amino-acid residues in SaFtsZ) and the 11 first N-terminal residues, which are absent from the crystal structure, were not included in the FtsZ polymer models. We constructed single filament models with variable curvature (Fig. S2) and length (Fig. S3), observing that the 0.14 $Å^{-1}$ peak disappears in curved filaments, then multiple straight filaments (Fig. S4) and finally multiple nontouching curved filaments (Fig. S5) that are required to simultaneously capture the ~0.05 $Å^{-1}$ and ~0.09 $Å^{-1}$ maxima and smooth higher angle region of the BsFtsZ polymers experimental profiles (see Supporting Material for a step-by-step description of model analysis of SAXS by FtsZ polymers). Models were combined with a 5% fraction of a similar number of unassembled FtsZ monomers, for better comparison with experimental profiles (BsFtsZ $Cr = 2.2$ μM, 4.4%). These models are exemplified by a triple filament, made of 70 Å laterally spaced off-plane curved filaments leaving a puzzling gap between them (Fig. 2 *B*; 3 × 60 monomers). Closing the curved models into rings generated evenly spaced ripples that were not experimentally observed; and straight filaments resemble less well the data. The central scattering by the models is less steep than by BsFtsZ-GMPCPP polymers, which indicates that the latter are still larger scattering objects, as also indicated by their turbidity in white light. We suggest that they form by aggregation or annealing of curved filament bundles, similar to those described by the models. We concluded from model analysis that the experimental BsFtsZ polymer SAXS can be explained by loose bundles of ≥3 curved protofilaments of variable length, laterally spaced 70 Å, and their aggregates. In contrast, the smooth scattering and the bulge at 0.143 $Å^{-1}$ of the tail-less tag-BsFtsZ-ΔCt-GMPCPP polymers are simulated by straight bundles of ≥2 touching protofilaments, which can be exemplified by a model made of three straight touching filaments at a 48 Å center-to-center distance (Fig. 2 *B*). We attributed the different spacing in tag-BsFtsZ-ΔCt to the deletion of the flexible C-terminal tail, which would span the gap between filaments in full-length BsFtsZ.

Time-resolved x-ray scattering by EcFtsZ and MjFtsZ polymers

We extended SAXS assembly experiments to polymers of different FtsZ proteins, Gram-negative bacterial EcFtsZ and archaeal MjFtsZ (Fig. 3). The EcFtsZ profiles were smoother, generally with fewer features than BsFtsZ. The steep central scattering indicated the formation of large polymers with GMPCPP, whose maximal dimensions were beyond measurement with our time-resolved synchrotron SAXS setup that hardly distinguished filament lengths above ~600 Å (as well as the static SAXS measurements by other authors using in house x-ray instrumentation (46)). However, the intermediate angle scattering ($q < 0.06$ $Å^{-1}$) was compatible with EcFtsZ forming long cylindrical rods 60–70 Å in diameter, according to linear modified Guinier plots of $\ln(q \cdot I(q))$ versus q^2 (47). There was an incipient shoulder at ~0.10 $Å^{-1}$ possibly generated by protofilament pairs, but a clear maximum at 0.05 $Å^{-1}$ as for BsFtsZ was not observed. On the other hand, increasing the EcFtsZ protein concentration to 125 μM permitted us to observe a maximum at 0.145 $Å^{-1}$ corresponding to a 43 Å axial monomer spacing along FtsZ protofilaments. Upon nucleotide exhaustion, the central scattering went down (Fig. 3, *inset*) without showing other prominent features. EcFtsZ polymers assembled with GTP (containing 53% GTP, 47% GDP) or with a GTP regenerating system (containing 80% GTP, 20% GDP) gave fewer marked scattering features than with GMPCPP, and a sample with GDP was similar to depolymerized samples after GTP hydrolysis (data not shown). The MjFtsZ polymer scattering was quite smooth, without prominent maxima except for the steep central scattering (Fig. 3). These characteristics suggested the formation by both EcFtsZ and MjFtsZ of long, one-FtsZ-molecule-wide filaments, with some lateral association between them under the conditions employed.

Model analysis of x-ray scattering by EcFtsZ protofilaments

We first constructed single filaments made of 140 FtsZ crystallographic monomers with different curvature angles (Fig. S2). Straight models have a sharp peak at 0.143 $Å^{-1}$

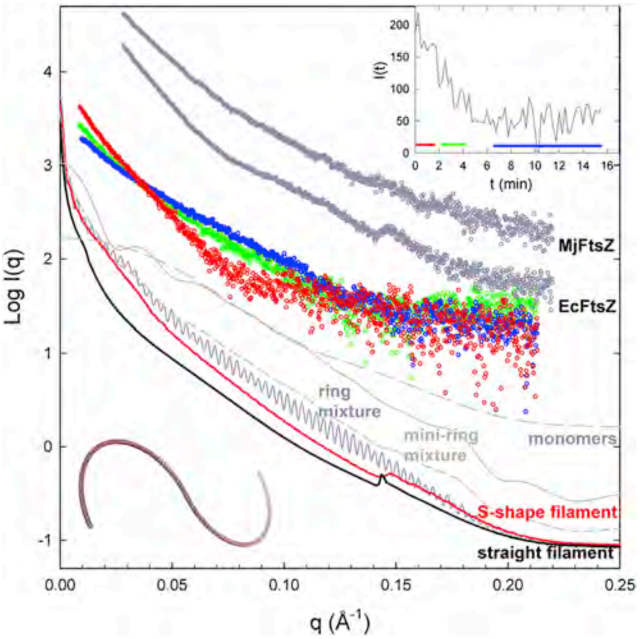

FIGURE 3 SAXS by EcFtsZ and MjFtsZ polymers and filament models. Polymers were assembled from EcFtsZ (50 μM) in PIPES 250 buffer with 10 mM $MgCl_2$ and 0.1 mM GMPCPP at 25°C. The red circles profile is an average of the initial time frames, the green one corresponds to disassembling polymers, and the blue one to the solution after disassembly, as indicated in the inset; an experiment using Tris 50 buffer gave similar results. Also shown (upshifted) are the scattering by polymers of EcFtsZ (125 μM) in PIPES 250 buffer and by MjFtsZ (50 μM) polymers in Mes50 buffer with 10 mM $MgCl_2$ and 0.2 mM GMPCPP at 55°C. The scattering profiles of representative models (from Figs S2 and S3), combined with a 5% of FtsZ monomers, are shown as indicated in the lower part of the figure. The scattering profile of unassembled FtsZ monomers is indicated by the dashed line, similarly to Fig. 2 *B*. The straight protofilament model (*solid line*) was made of 140 SaFtsZ monomers. The closed ring mixture contains 30% of 100 monomer rings, 40% of 120 monomer rings, and 30% of 140 monomer rings (*dark shaded line*). The mini-ring mixture contains 30% of 14 monomer rings, 40% of 16 monomer rings, and 30% of 18 monomer rings (*light shaded line*). The shaded short dashed line below it is a mixture of 20% FtsZ in mini-rings and 80% in S-shape filaments. The S-shape model shown is made from two semicircles of 60 monomers each with 3.5 and −3.5° bending angles between consecutive monomers (end-to-end distance 3360 Å), which was chosen to exemplify protofilaments of variable curvature and length (Figs. S1 and S2). To see this figure in color, go online.

that is reduced in curved models, and these have undulations at higher angles that tend to cancel out by mixing models with different curvatures. As the filaments curve beyond a semicircle and approach ring closure, a series of sinusoidal ripples with an ~0.003 Å^{-1} period appear throughout the model scattering profile, corresponding to the subsidiary maxima of a J_0-like Bessel function arising from rings with mean diameter ~2000 Å, the period being inversely proportional to the ring diameter (48). Combining rings of close sizes (100, 120, and 140 monomers) hardly smoothed the ripples, which are absent from the experimental data (Fig. 3). Mini-rings made of 16 monomers (224 Å diameter) give a sinusoidal pattern with a longer period (~0.03 Å^{-1}). Combining mini-rings of close sizes (14, 16, and 18 monomers) smoothed the model scattering profile in the middle region, leaving some periodic features in the low- and high-angle zones (Fig. S2). Varying the filament length at constant curvature (Fig. S3) showed that the ~0.14 Å^{-1} maximum is more marked in models covering circular arches up to 80° and disappears in the longer models. These have undulations and ripples that smooth out by combining open filaments of close sizes, or in certain individual S-shape models. The model filament scattering curves were combined with 5% (EcFtsZ $Cr = 2.2$ μM, 4.4%) of scattering by unassembled FtsZ monomers. This procedure softens the 0.14 Å^{-1} maximum of straight models and the higher angle undulations of curved models, making their corresponding model mixtures qualitatively compatible with the EcFtsZ polymers experimental data (Fig. 3); however, this is clearly not the case for ring model mixtures, in which the characteristic oscillations remain at low and mid-angles after mixing with FtsZ monomers. The amplitude of these oscillations clearly exceeds experimental noise. For example, the oscillations of ring model mixture scattering intensity at 0.12 Å^{-1} have a relative amplitude (±26%) five times larger than the normalized SD (5%) of the scattering by the more concentrated EcFtsZ sample (Fig. 3). We concluded from the model analysis that the experimental EcFtsZ polymer SAXS is compatible with single filament FtsZ models of variable curvature and length. Such ensemble of FtsZ filament configurations may include S-shapes, as in the model shown (Fig. 3), as well as less curved S- and C-shapes, and multiple filaments should not be excluded. However, a predominant population of large rings of close sizes is incompatible with the EcFtsZ SAXS data, although we could not rule out filament tangles. A small proportion of FtsZ subunits forming mini-rings (20%) among curved filaments (80%) would be qualitatively compatible with the results (Fig. 3).

Cryo-electron microscopy of full-length and tail-less BsFtsZ polymers

After the SAXS analysis of the bulk structural features of FtsZ polymers in solution, to obtain structural information of individual FtsZ assemblies, we examined the polymers formed by full-length and tail-less BsFtsZ constructs under identical conditions (50 μM FtsZ) by cryo-EM of frozen hydrated samples without any support or stain. We found that BsFtsZ with GMPCPP forms curved protofilaments (~40 Å wide) that frequently coalesce into spirals or toroids (~1600 Å in diameter), forming large aggregates (Fig. 4 *A*). The BsFtsZ toroids, previously observed in negative stain (35), thus form in the solution rather than onto the carbon surface of the EM grids. The fact that the strong periodic SAXS features characteristic of toroidal stacked FtsZ ring models (Fig. S5) were not detected (Fig. 2) suggests that the toroids are relatively disordered, formed by loosely

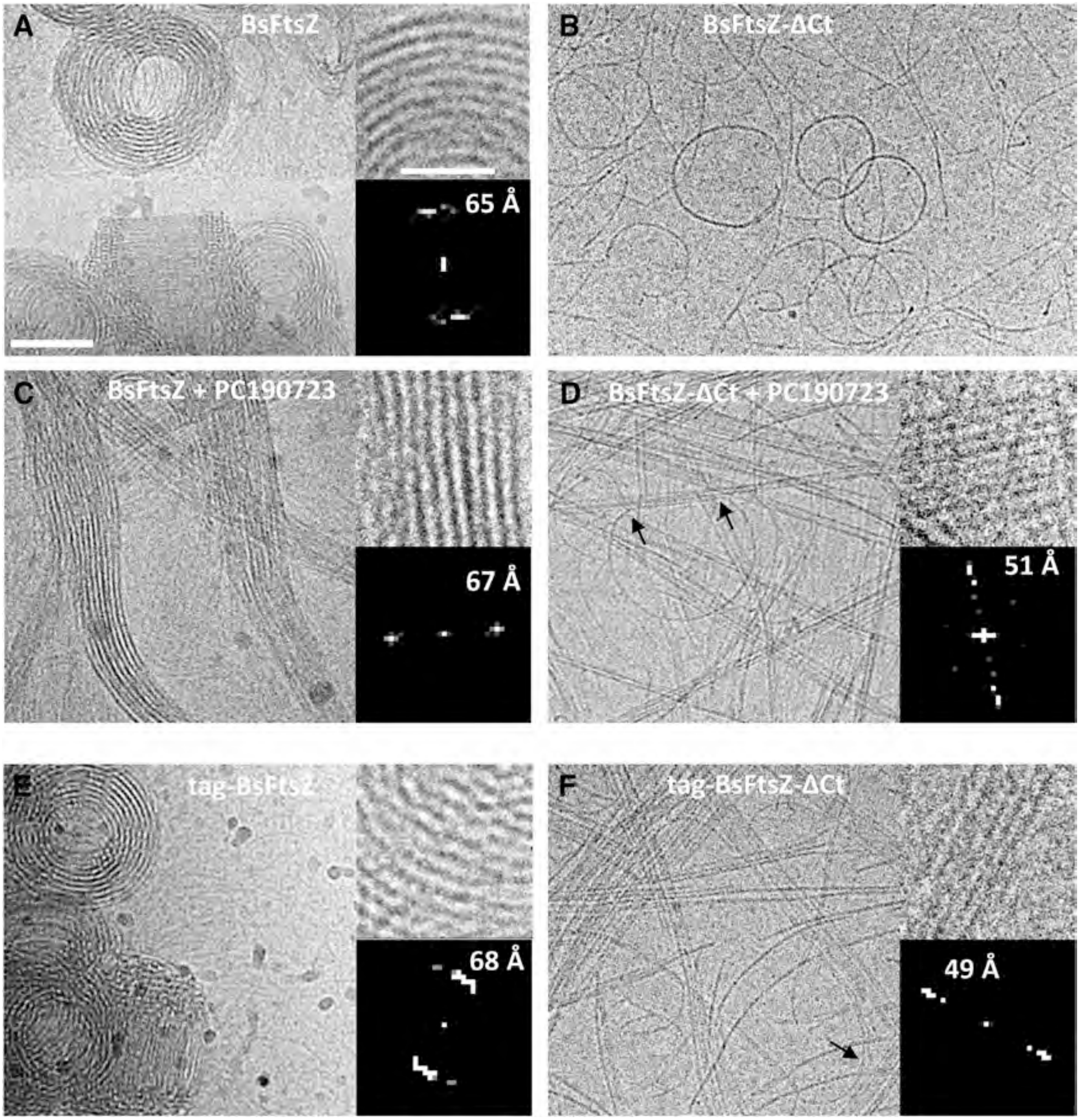

FIGURE 4 Cryo-EM of BsFtsZ and BsFtsZ-ΔCt polymers. 50 μM BsFtsZ (*A* and *C*) and BsFtsZ-ΔCt (*B* and *D*) were assembled in Tris 50 buffer with 10 mM $MgCl_2$ and 0.1 mM GMPCPP at 25°C, in the absence or presence of 20 μM PC190723, and polymers formed were visualized by cryo-EM. Tag-BsFtsZ (*E*) and tag-BsFtsZ-ΔCt polymers (*F*) were also examined. Arrows (*D*) and (*F*) indicate single filaments coming out from bundles. Bar, 1000 Å. The insets in each case are enlarged areas (bar, 500 Å) and their computed diffractograms where the spacing of the main equatorial spots is indicated.

associated protofilaments. In striking contrast with the full-length protein, untagged C-terminally truncated BsFtsZ-ΔCt (BsFtsZ(1–318)) assembled weakly in light scattering and sedimentation tests, forming single protofilaments with variable curvature and circles (Fig. 4 *B*, ~1000 Å in diameter). Adding the FtsZ polymer-stabilizing ligand PC190723 resulted in the formation of large BsFtsZ bundles (Fig. 4 *C* and (35)) and more efficient assembly of BsFtsZ-ΔCt forming straight bundles and single curved filaments that frequently came out from the bundles (Fig. 4 *D*). Tag-BsFtsZ assembled similarly to BsFtsZ (Fig. 4 *E*), whereas tag-BsFtsZ-ΔCt formed straight protofilament bundles as well as curved single filaments (~40 Å wide) that frequently came out from straight ends (Fig. 4 *F*); the bundles were typically longer than the 1 μm diameter of the cryo-EM grids holes. We also observed similar long straight bundles in negatively stained samples (Fig. S6). The cryo-EM results thus support the SAXS model analysis of the distinct types of polymers formed by BsFtsZ and tag-BsFtsZ-ΔCt (Fig. 2), permitting the observation of the toroids and bundles, respectively, with dimensions larger than measurable with our SAXS setting. Assembly with GTP gave similar results as with GMPCPP, curved filaments and toroids of BsFtsZ and tag-BsFtsZ, and straight bundles with tag-BsFtsZ-ΔCt (Fig. S7, *A–C*). We inferred from these results that the C-terminal tail is required for efficient BsFtsZ assembly and bundling (compatible with some previous observations (49)), which can be rescued in the tail-less proteins by the known binding of PC190723 to FtsZ polymers (27,35), or the by added N-terminal tag residues GSHMAS making currently uncharacterized bundling interactions.

Interestingly, computed diffraction patterns from apparently flat zones of full-length BsFtsZ toroids and bundles showed an equatorial reflection corresponding to a 65–67 Å lateral spacing between protofilaments (Fig. 4, *A* and *C*), whereas the tail-less BsFtsZ bundles showed a main spot corresponding to 49–51 Å and minor ones corresponding to longer distances (Fig. 4, *D* and *F*, with GMPCPP); measurements with GTP gave a similar 68.5 ± 2.5 Å distance for the full-length protein and 55 Å distance for the tail-less construct (Fig. S7, *A* and *B*). These cryo-EM spacings, which were somewhat dependent on image sampling (Fig. S7 *D*), are compatible with the 70 and 48 Å distances between BsFtsZ and tag-BsFtsZ-ΔCt protofilaments, respectively, estimated by SAXS analysis. Measuring center-to-center distances between neighbor protofilaments from density profiles resulted in clearly different distributions ($p < 0.01$), with full-length BsFtsZ average 66–70 Å and truncated protein average 55–58 Å, with GMPCPP and GTP (Fig. S7, *E* and *F*). These measurements support the loose lateral association of the wild-type filaments and a closer lateral contact of monomers from neighbor filaments of the truncated protein. This may explain why the wild-type filament bundles curve, but the truncated protein filaments are held straight in bundles and bend only when isolated.

Cryo-EM of disassembling BsFtsZ polymers upon nucleotide consumption did not show any prominent intermediate morphologies but revealed the formation of end products consisting of highly curved oligomers and mini-rings, also observed with GMPCP or GDP (Fig. S8); the more abundant mini-rings formed by EcFtsZ are characterized below.

Effects of CTC-CTV deletion and varying CTL length on BsFtsZ polymers

To dissect the roles of the C-terminal end (CTC-CTV) and the long intrinsically disordered linker (CTL) on FtsZ polymers architecture, we tested with cryo-EM six additional BsFtsZ C-terminal constructs previously characterized in vitro and in vivo (36,49; Table S1). Several of these proteins assembled more weakly than native BsFtsZ, but efficient assembly was restored by PC190723. BsFtsZΔC17 (BsFtsZ(1–365)), lacking CTC and CTV, rendered frequently associated curved filaments, with a spacing between them of 65–67 Å (Fig.S9, *A* and *B*), similar to full-length BsFtsZ. We interpreted that the CTC-CTV is not an absolute requirement for bundle formation under our high concentration conditions and that the CTL spans the gap between the filament cores. BsFtsZ-ΔCTL25 (a deletion of the last 25 CTL residues leaving the CTC-CTV that supports cell division), gave 62–65 Å spaced protofilaments (Fig. S9, *C* and *D*) with a similar morphology to the native protein. In contrast, BsFtsZ-ΔCTL50 (a nonfunctional deletion of the whole CTL leaving CTC and CTV) assembly resulted in the formation of straight bundles, similar to tag-BsFtsZΔCt, with a spacing of 55 Å (Fig. S9, *E* and *F*). We then examined the effects of replacing the native CTL in BsFtsZ with three segments of increasing length from the CTL from *Agrobacterium tumefaciens* FtsZ. BsFtsZ-CTLA50, which has a 50-residue linker (with same length as the native BsFtsZ linker but different sequence; functional in vivo) formed bundles of protofilaments spaced each 68 and 80 Å (Fig. S10, *A* and *B*). Fittingly, BsFtsZ-CTLA100 (100-residue linker; supporting cell division) gave relatively looser bundles with spacings of 86 and 95 Å (Fig. S10, *C* and *D*). Finally, BsFtsZ-CTLA249 (249-residue linker; no longer functional in vivo) formed quite disordered curved bundles that gave irregular diffractograms in which some weak spots corresponding to longer distances could still be observed (~100–145 Å; Fig. S10, *E* and *F*). The cryo-EM results taken together support the notion that the C-terminal tail provides the spacing between FtsZ filaments, in a proportion of 0.31–0.38 Å per amino-acid residue excluding BsFtsZ-CTLA249 (Fig S10, *G* and *H*).

Cryo-electron microscopy reveals curvature of disassembling EcFtsZ filaments

We also examined the morphology of EcFtsZ polymers by cryo-EM under the same solution conditions as in the SAXS measurements. EcFtsZ has less tendency to curve and bundle than BsFtsZ. Steady-state EcFtsZ-GTP polymers have been previously studied with cryo-EM (31,50) and the formation of straight bundles of C-terminally truncated EcFtsZ (1–320) was reported in an early study with negative stain (51). Therefore, we mainly focus here on the morphology of EcFtsZ filaments during disassembly, revealing a sequence of progressively curved filaments in cryo-EM that had not been detected by the bulk SAXS measurements.

The assembly time course of EcFtsZ (50 μM, with 1 mM GTP or 0.1 mM GMPCPP) was monitored by light scattering (Fig. 5 *A*). Samples at times of maximal scattering and during disassembly upon nucleotide consumption were taken on holey grids and immediately vitrified. Straight bundles, filament pairs, and some long single filaments of variable curvature were observed at maximal scattering with GTP. The EcFtsZ protofilaments in the bundles were separated at variable distances, including 68 Å (Fig. 5 *B*), rather than in lateral contact. Our cryo-EM images are too crowded to estimate filament flexibilities and discriminate between reported differences in flexibility of EcFtsZ single filaments at low concentrations, with persistence length values in the ranges of 1000 Å (31) or

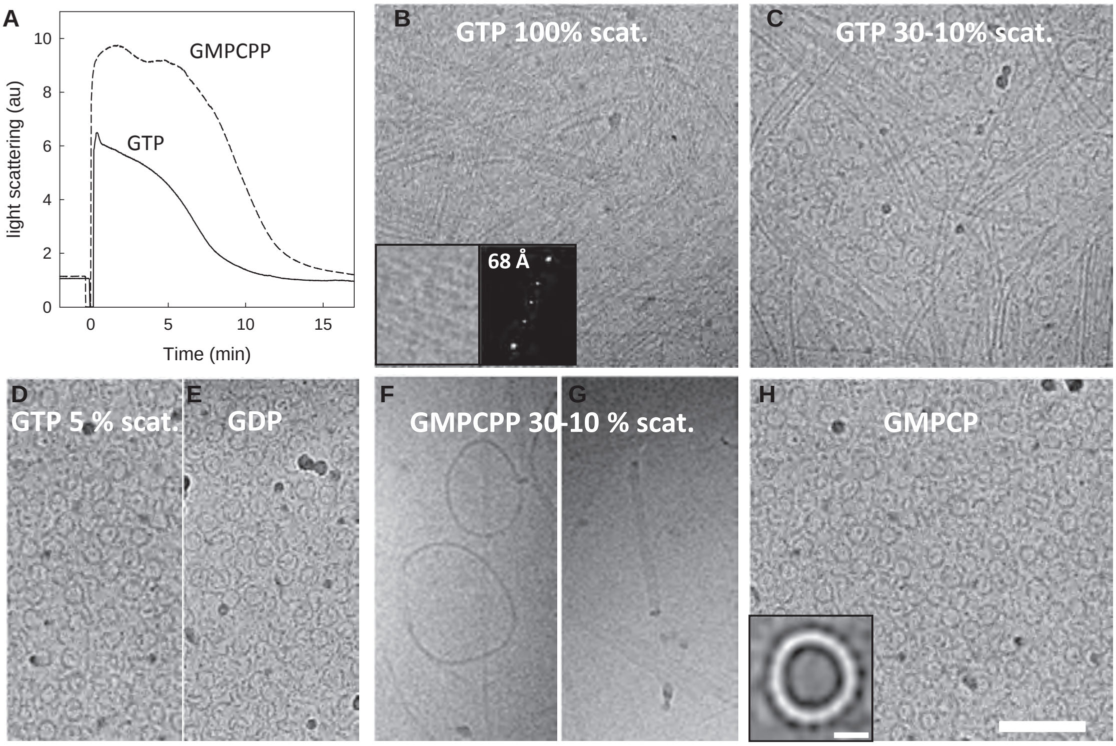

FIGURE 5 Cryo-EM of disassembling EcFtsZ polymers. (*A*) Shown here are light scattering time courses of 50 μM EcFtsZ assembly in PIPES 250 buffer with 10 mM $MgCl_2$, and 0.1 mM GMPCPP or 2 mM GTP; nucleotides were added at zero time. Samples were taken at different stages of polymerization and observed by cryo-EM. (*B*) Shown here is EcFtsZ assembled with GTP at maximum light scattering; the inset shows an enlarged bundle and its corresponding diffractogram, showing a main equatorial spot at 68 Å. (*C*) Shown here is 30–10% light scattering. (*D*) Shown here is 5% light scattering. (*E*) Shown here is EcFtsZ with 1 mM GDP. (*F* and *G*) Representative circular structures were observed during depolymerization with 0.1 mM GMPCPP (30–10% light scattering; these particular samples were made at 4 μM EcFtsZ). (*H*) Shown here is EcFtsZ with 0.1 mM GMPCP. Bar, 1000 Å. The inset shows an image (contrast inverted) of a predominant mini-ring class average (220 Å in diameter, 16 monomers; bar, 100 Å) after classification of 2154 mini-ring particles with SCIPION (Materials and Methods); the diameter was very similar in each class.

1.4 μm (50). The proportion of curved filaments apparently increased as scattering decreased to 30–10% (Fig. 5 *C*). At 5% of initial scattering C-shape oligomers and ~220 Å diameter mini-rings were frequently observed (Fig. 5 *D*). Supporting mini-ring formation upon GTP hydrolysis, similar objects formed from not previously assembled EcFtsZ-GDP (Fig. 5 *E*).

Similar results were obtained with GMPCPP, but we also observed at 30–10% scattering a small proportion of large rings with diameter 1480 ± 490 Å (Fig. 5 *F*), corresponding to 106 ± 35 FtsZ monomers. Their width in flat view was ~50 Å, but side views showed 100–150 Å widths fitting with double/triple ring structures or flat helices (Fig. 5 *G*), probably formed by curved filament annealing. These rings had not been detected by SAXS during EcFtsZ disassembly, possibly due to their low abundance. Mini-rings were frequently observed upon GMPCPP consumption at 5% of initial scattering, or directly with GMPCP (diameter was similar to GDP mini-rings). Image analysis indicated rings with mean diameter of 220 ± 5 Å, corresponding to 16 EcFtsZ subunits spaced each 43 ± 1 Å (Fig. 5 *H*). For comparison, we made similar experiments with negatively stained samples on carbon-coated grids (Fig. S11, *A* and *B*), and found more irregularly curved filaments, some of them circular, in the disassembling EcFtsZ samples (Fig. S11, C and *D*), suggesting large rings deformation and opening by adsorption to the carbon support. Highly curved C-shape objects and mini-rings were also observed in negatively stained samples (Fig. S11 *E*).

The FtsZ mini-rings observation by cryo-EM but not by SAXS may be explained by sample heterogeneity (mini-ring mixture in Fig. 3). Cryo-EM observations reveal structural characteristics of existing objects in the sample, but whose ratio may not represent their actual proportion in the solution. Mini-rings images really represent a fraction of the protein over a heterogeneous background of oligomers of different sizes and curvatures (Fig. 5 *H*) that may further obscure their periodic SAXS features. On the other hand, a major potential artifact during cryo-EM sample vitrification is the disassembly of macromolecular complexes, thought to occur because of the forces between molecules confined within a thin layer of vitrified ice, or by their interactions with the air-water interface for the short period after blotting but before vitrification. Nonetheless, the physics of the process is poorly understood. In a typical experiment, a labile macromolecular complex can produce several subcomplexes in the cryo-EM grids, which can be found in areas of thinner ice, whereas thicker ice is more likely to contain the intact assembly. Cryo-EM preparation is optimized for each sample to reduce these undesired effects, by tuning blotting and buffer conditions. Also, new methodological approaches are being explored to reduce disassembly of complexes in cryo-EM (52). In our case, employing complementary analytical ultracentrifugation experiments under identical nonpolymerizing conditions with GDP or GMPCP, we observed a series of increasing and abruptly ending sedimentation velocity boundaries (~3 S, 4.5 S, 6 S, and 7S; Fig. S12); this is expected from a fast reversible Mg^{2+}-induced self-association of monomers with formation of ring end-products, at intermediate protein concentrations (53), which supports the cryo-EM mini-ring observations.

DISCUSSION

FtsZ filaments bending upon nucleotide hydrolysis

Our cryo-EM results suggest that steady-state FtsZ filaments have different intrinsic curvatures depending on the EcFtsZ or BsFtsZ species, perhaps related to their different C-terminal tails. Interestingly, FtsZ filaments further bend upon nucleotide consumption, permitting the consecutive observation of a small fraction of large circles (1000–2000 Å mean diameter) and somewhat more abundant highly curved mini-rings later on (220 Å diameter), which had not been detected by SAXS. We think that rings formation reflects FtsZ filament curvature in solution upon nucleotide hydrolysis, which is shown here using solutions vitrified for cryo-EM observation. FtsZ filament curvature after GTP hydrolysis had been reported in negatively stained samples (54,55); however, adsorption to the carbon support of the EM grid can modify the structure of the polymers; for example, CcFtsZ was reported to form curved filaments that convert to larger straight bundles in seconds after contact with the carbon surface (56). Carbon surface effects on the structure and assembly of complexes have been frequently observed and some methods have been developed to try overcoming this problem, such as a mild gradient fixation method, GraFix, that reduces dissociation of particles during sample preparation (57). Another well-known effect of carbon support films is that they can have more affinity for certain complexes or conformation in the sample, and thus, the ratio of species or conformations on the EM grid does not necessarily represent the ratio found in the original solution.

The curvature of the large circles that we have observed in depolymerizing EcFtsZ (2.5–5° bending angle between consecutive subunits) corresponds to the so-called intermediately curved filaments, which were hypothesized to generate constriction force in dividing bacterial cells (25). However, taking into account their relatively low abundance, we find more likely that they form by limited end-to-end annealing of filaments that become more flexible upon partial nucleotide hydrolysis along them. In our view, a possible molecular mechanism for FtsZ filament bending, after nucleotide hydrolysis and before disassembly, is the reversible opening of the association interface between consecutive subunits in the GDP-bound state; this state lacks a stabilizing coordinated Mg^{2+} ion, as observed in molecular dynamics (MD) simulations of SaFtsZ filaments (29).

Several studies reported sharp fast sedimenting boundaries in polymerizing EcFtsZ solutions and proposed the predominant formation of a narrow distribution of large closed cyclic filaments (58–60), made of 80–120 FtsZ monomers with GTP and 140–180 monomers with GMPCCP (61). However, our SAXS results practically exclude a majority of large regular rings with a narrow size distribution (Fig. 3); and a majority of such closed filaments, being they rings or irregular tangles, would be at odds with the predominantly elongated EcFtsZ filament morphology observed in cryo-EM (Fig. 5; (31,50)), as well as with FtsZ directional treadmilling (22,23). On the other hand, AFM studies of EcFtsZ polymers directly adsorbed on mica showed dynamic filaments forming bundles and multiple intermediately curved rings (62). Depolymerizing EcFtsZ filaments on a mica surface formed curved filaments and closed rings made of 103 ± 26 monomers with GTP and 137 ± 32 monomers with GMPCPP that were quite stable and opened before rapidly depolymerizing (63). However, the claimed similarity of these values to the number of monomers estimated for FtsZ polymers in solution (60) may be coincidental, because the mica surface promotes FtsZ assembly (64). We think that mica adsorption may favor formation of large curved FtsZ structures in a process physically different from membrane-tethered FtsZ assembly. We pursued observation of large cyclic EcFtsZ polymers with SAXS and cryo-EM but did not find them in steady-state FtsZ polymer solutions. Only in depolymerizing EcFtsZ-GMPCPP samples, we observed cryo-EM rings made of 106 ± 35 monomers per turn (Fig. 5).

Assembly inactive FtsZ forms highly curved association interfaces

FtsZ mini-rings have a high curvature (22.5° bending between subunits), which was thought not to spontaneously take place but was observed in negative stain after adsorption onto cationic lipid monolayers (65) or in EcFtsZ tubes formed with DEAE-dextran (54) and more recently with ZipA and FtsA* (66). We have now observed EcFtsZ mini-rings in vitrified solutions with cryo-EM, in depolymerizing EcFtsZ and BsFtsZ samples, as well as with GDP or GMPCP, using relatively high protein concentrations. We suggest that highly curved oligomers and mini-rings are association products of inactive nucleotide-diphosphate-bound FtsZ proteins. The mini-rings curvature appears striking, considering the crystal structure of straight

SaFtsZ-GDP filaments (28) and their limited bending in unrestrained MD simulations (6.6 ± 4.4° bending angle (29)). However, in both cases, the subunits have their interdomain clefts open and form tight association interfaces. In contrast, very recent SaFtsZ monomer structures have shown the inactive conformation, which has the interdomain cleft closed and forms incomplete pseudo-interfaces that are incompatible with straight filament assembly (33). Supportingly, *Mycobacterium tuberculosis* FtsZ (30) and MjFtsZ (67) closed-cleft FtsZ structures were observed to form open interfaces. We would thus expect the interdomain clefts to be closed in mini-rings.

Filament curvature and the formation of ring structures are recurrent themes in FtsZ and tubulin research (48,65,66,68). We regard mini-rings as in vitro self-association end-products of each inactive GDP-bound protein form that provide mechanistic insight into their function, rather than forming with a GTP excess in cells. Thus, FtsZ·GDP forms 220 Å single rings (this work), whereas tubulin·GDP forms 380 Å-diameter double rings, whose SAXS solution structure (48) is equivalent to coiled protofilaments from microtubules. Protofilament curling at depolymerizing microtubule ends (69) relates to the tendency of tubulin subunits to adopt a curved conformation characteristic of their relaxed assembly inactive state (48,70), which contributes to microtubule dynamics (71). GDP-bound SaFtsZ filaments curve with the C-termini toward the inside in MD simulations (29), in a direction similar to curling tubulin protofilaments at microtubule ends. Thus, FtsZ and tubulin protofilaments may curve, employing different mechanisms, in roughly similar directions upon nucleotide hydrolysis. Notice, however, that the intrinsic curvature of GTP-bound SaFtsZ filaments has an opposite direction, with the C termini outside in the MD simulations, which we think may explain liposome constriction by FtsZ-Mts (17,72) even without GTP hydrolysis (18) as well as the observation of large C-terminal fusions outside FtsZ spiral tubes with DEAE-dextran (73).

BsFtsZ forms loose bundles of curved filaments held 70 Å apart by the flexible C-terminal tails

We propose that the lateral center-to-center spacing that we have observed with SAXS (70 Å) and cryo-EM (68.5 ± 2.5 Å) between curved BsFtsZ filaments forming loose bundles is provided by the intrinsically disordered CTL spanning the gap between protofilament cores. This is supported by 1) the close contact (48–50 Å spacing) between the FtsZ core structures from neighbor filaments in two types of whole C-tail deleted BsFtsZ polymers; 2) the spacing (65–67 Å) between filaments in bundles with CTL but deleted CTC-CTV; 3) the spacings observed proportional to the C-terminal length; and 4) the difficulty in conceiving how any other part of FtsZ could span the gap between filaments, which can be estimated as ∼20 Å for ∼50 Å thick filaments. Parallel filaments of tail-less BsFtsZ possibly stick to each other, generating the observed straight bundles, whereas in the full-length BsFtsZ filament, curvature is allowed by flexible lateral association. Comparison with tubulin shows that whereas microtubules are made of protofilaments in lateral contact forming an ordered lattice with the C-terminal ends at the microtubule surface, FtsZ forms bundles of protofilaments loosely bridged by their disordered C-terminal linkers. Notice that the C-terminal extension may reach distances comparable to the size of the FtsZ structured core. Modeling the disordered 50-amino-acid C-terminal linker of EcFtsZ as a wormlike chain predicted an entropic spring with an average end-to-end distance of 44 Å, whereas for the complete C-terminal extension (72-amino-acid) a value of 52 Å (0.72 Å per amino acid) was measured by Förster resonance energy transfer, in the absence of any stretching or compression force (37). The latter value could give, together with a 48 Å filament thickness, a center-to-center spacing between filaments of 100 Å. This distance may be reduced by multiple electrostatic interactions of the extreme C-termini from each filament with the neighbor filaments in a bundle (36) or at high protein concentrations as in BsFtsZ-ΔC17 (Fig. S9, *A* and *B*). The spontaneous twist of FtsZ filaments, estimated as an angle of −10.2° ± 2.8° between consecutive GTP-bound monomers from molecular dynamics simulations (29), would prevent back-to-back protofilament contact in solution. In contrast, close protofilament pairs with the C tails likely pointing outwards were observed by electron microscopy of artificial calcium-induced sheets of His-tagged FtsZ (44) and also in negatively stained FtsZ polymers (74), where it is possible that the C tails collapse by adsorption to the carbon support or with the staining agent, facilitating close protofilament association.

A role for the FtsZ disordered C-tail in the structural dynamics of the Z-ring

The flexible FtsZ C-terminal tail plays a critical role in bacterial cell division, mediating electrostatic interactions between FtsZ filaments, interactions with membrane attachment and regulatory proteins, and correct cell-wall cross-linking during division (36–39). We propose that multiple weak lateral interactions provided by the C-terminal tails, reversibly connecting protofilaments in loose FtsZ bundles (Fig. 6), underlie assembly of the dynamic Z-ring clusters observed by SR fluorescence microscopy. EcFtsZ bundles in vitro more weakly than BsFtsZ, but EcFtsZ filament bundling in cells may be modulated by associated proteins such as Zap (12). It is tempting to speculate that the 70 Å spacing that we observe between FtsZ protofilaments in solution recapitulates the similar spacing between single FtsZ filaments observed in different bacterial cells and in liposomes by electron cryotomography (15,16). Hypothetical protofilament sliding during Z-ring constriction was thought

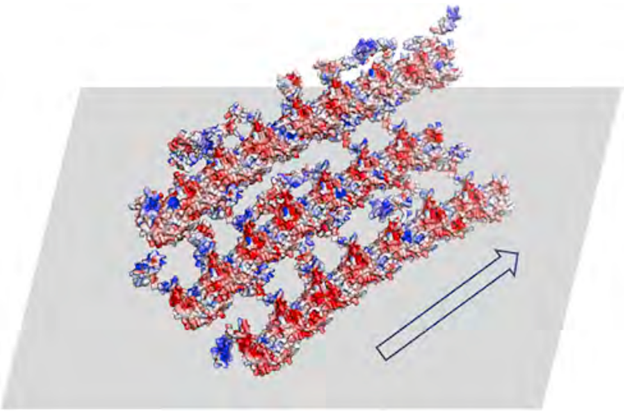

FIGURE 6 Illustrative model scheme for part of a FtsZ filament cluster. An enlarged fragment of the curved triple filament model from Fig. 2 *B* is shown after adding the C-terminal tails (Materials and Methods). Several of the tails bridge protofilaments, whereas others point toward the back for tethering to the membrane (*shaded surface*) or in other directions to bind bundling proteins (omitted here for simplicity). The protein electrostatic contact potential is displayed. Treadmilling is indicated by the arrow with an arbitrary polarity. To see this figure in color, go online.

to require breaking all lateral bonds first, a very slow process predicted not to take place within the timescale of bacterial cell division (24); flexible tethering would solve this problem, permitting protofilaments to slide with respect to one another without being released from a bundle. However, short FtsZ filaments, rather than complete rings, can drive asymmetric peptidoglycan synthesis and cell envelope constriction at the onset of cytokinesis (75).

Recently, break-through fluorescent imaging, genetic experiments, and biochemical experiments combined have shown that cellular FtsZ assemblies exhibit treadmilling dynamics coupled to GTPase activity (rather than sliding), moving in both directions around the division ring, which guides septal cell wall synthesis and bacterial division in *E. coli* (76) as well as in *B. subtilis* (77). The estimated size distribution of dynamic FtsZ clusters in *E. coli* cells averages to 683 ± 439 (mean ± SD) FtsZ molecules (76), suggesting multiple FtsZ filaments as in the smaller clusters observed by SR imaging (12). In addition, the chirality of clockwise-rotating vortices assembled from FtsZ-Mts on flat supported membranes has been recently explained by three orthogonal directions of filament polar growth, membrane attachment, and curvature (23). Actually, curved filaments moving along chiral circular paths on a membrane are predicted to self-organize into vortex patterns at intermediate particle densities (78). The intrinsic curvature of FtsZ filaments thus appears to be an essential property for treadmilling of membrane-attached FtsZ filament bundles. The clockwise rotation of FtsZ vortexes in the reconstituted systems is, however, in contrast with the bidirectional movement of FtsZ clusters in cellular Z-rings. It is conceivable that loose connections between curved FtsZ protofilaments through the flexible C-tails (Fig. 6) may facilitate their directionally coherent treadmilling for the movement of membrane-tethered assemblies (22,23,76). Reversible association through the intrinsically disordered C-terminal linker, filament curvature, and twist, possibly prevent FtsZ filaments from rigidly sticking to each other and ensure the required functional flexibility in bacterial cells. In this type of model, steady-state FtsZ filaments curve parallel to the inner membrane (23) and coalesce into FtsZ clusters that treadmill to drive correct septal cell wall synthesis (76,77), rather than curving perpendicular to the membrane to generate constriction force. FtsZ filament bending by GTP hydrolysis, likely in an opposite direction, might instead be involved in FtsZ filament turnover, cluster remodeling, and signal processing (79) during bacterial cell division.

SUPPORTING MATERIAL

Supporting Materials and Methods, twelve figures, and one table are available at http://www.biophysj.org/biophysj/supplemental/S0006-3495(17)30969-4.

AUTHOR CONTRIBUTIONS

S.H. was a main author, and performed biochemical analysis and cryo-EM. E.R.A. was a main author, and performed SAXS analysis and model building. A.V., R.N.R., O.L., J.F.D., and J.M.A. performed research and analyzed data. D.J.R. and P.C. contributed all FtsZ proteins. M.A.O. contributed the BsFtsZ-ΔCt plasmid. J.M.A. designed research and wrote the manuscript with input from all authors.

ACKNOWLEDGMENTS

We thank the ALBA BL11 team and ERSF BM29 beam line for SAXS facilities; C. Contreras-Martel and A. Dessen (IBS, Grenoble) for hosting AV and for access to ESRF; P. J. Buske and P. Levin for generously providing the expression plasmids for BsFtsZ-ΔC17, −ΔCTL25, −ΔCTL50, −CTLA50, −CTLA100, and −CTLA249; F. J. Gueiros-Filho for the pAB20 plasmid encoding His-tagged BsFtsZ; L. Araújo-Bazán for molecular microbiology support; J. R. Luque and C. Alfonso for sedimentation velocity; and P. Schuck, J. García de la Torre, and P. Chacón for discussions.

This work was supported by grants from the Ministry of Economy and Competitiveness (MINECO) BFU2014-51823-R (to J.M.A.), SAF2014-52301-R (to O.L.), and BFU2016-75319-R (to J.F.D.); a European Molecular Biology Organization (EMBO) fellowship ALTF-171-2005 (to M.A.O.); São Paulo Research Foundation (FAPESP) grants 13/26897-7 and 10/51870-7 (to P.C).; and doctoral contracts from Consejo Superior de Investigaciones Científicas-Junta para la Ampliación de Estudios (CSIC-JAE) (to E.R.A.) and Formación de Personal Investigador (FPI) (to A.V.).

REFERENCES

1. Bi, E. F., and J. Lutkenhaus. 1991. FtsZ ring structure associated with division in *Escherichia coli*. *Nature*. 354:161–164.
2. Xiao, J., and E. D. Goley. 2016. Redefining the roles of the FtsZ-ring in bacterial cytokinesis. *Curr. Opin. Microbiol.* 34:90–96.
3. Söderström, B., and D. O. Daley. 2017. The bacterial divisome: more than a ring? *Curr. Genet.* 63:161–164.

4. Haeusser, D. P., and W. Margolin. 2016. Splitsville: structural and functional insights into the dynamic bacterial Z ring. *Nat. Rev. Microbiol.* 14:305–319.
5. den Blaauwen, T., L. W. Hamoen, and P. A. Levin. 2017. The divisome at 25: the road ahead. *Curr. Opin. Microbiol.* 36:85–94.
6. Fu, G., T. Huang, …, J. Xiao. 2010. In vivo structure of the *E. coli* FtsZ-ring revealed by photoactivated localization microscopy (PALM). *PLoS One.* 5:e12682.
7. Strauss, M. P., A. T. F. Liew, …, E. J. Harry. 2012. 3D-SIM super resolution microscopy reveals a bead-like arrangement for FtsZ and the division machinery: implications for triggering cytokinesis. *PLOS Biol.* 10:e1001389.
8. Biteen, J. S., E. D. Goley, …, W. E. Moerner. 2012. Three-dimensional super-resolution imaging of the midplane protein FtsZ in live *Caulobacter crescentus* cells using astigmatism. *ChemPhysChem.* 13:1007–1012.
9. Rowlett, V. W., and W. Margolin. 2014. 3D-SIM super-resolution of FtsZ and its membrane tethers in *Escherichia coli* cells. *Biophys. J.* 107:L17–L20.
10. Holden, S. J., T. Pengo, …, S. Manley. 2014. High throughput 3D super-resolution microscopy reveals *Caulobacter crescentus* in vivo Z-ring organization. *Proc. Natl. Acad. Sci. USA.* 111:4566–4571.
11. Jacq, M., V. Adam, …, C. Morlot. 2015. Remodeling of the Z-ring nanostructure during the *Streptococcus pneumoniae* cell cycle revealed by photoactivated localization microscopy. *MBio.* 6:e001108–e001115.
12. Buss, J., C. Coltharp, …, J. Xiao. 2013. In vivo organization of the FtsZ-ring by ZapA and ZapB revealed by quantitative super-resolution microscopy. *Mol. Microbiol.* 89:1099–1120.
13. Lyu, Z., C. Coltharp, …, J. Xiao. 2016. Influence of FtsZ GTPase activity and concentration on nanoscale Z-ring structure in vivo revealed by three-dimensional superresolution imaging. *Biopolymers.* 105:725–734.
14. Si, F., K. Busiek, …, S. X. Sun. 2013. Organization of FtsZ filaments in the bacterial division ring measured from polarized fluorescence microscopy. *Biophys. J.* 105:1976–1986.
15. Li, Z., M. J. Trimble, …, G. J. Jensen. 2007. The structure of FtsZ filaments in vivo suggests a force-generating role in cell division. *EMBO J.* 26:4694–4708.
16. Szwedziak, P., Q. Wang, …, J. Löwe. 2014. Architecture of the ring formed by the tubulin homologue FtsZ in bacterial cell division. *eLife.* 3:e04601.
17. Osawa, M., D. E. Anderson, and H. P. Erickson. 2008. Reconstitution of contractile FtsZ rings in liposomes. *Science.* 320:792–794.
18. Osawa, M., and H. P. Erickson. 2011. Inside-out Z rings—constriction with and without GTP hydrolysis. *Mol. Microbiol.* 81:571–579.
19. Milam, S. L., M. Osawa, and H. P. Erickson. 2012. Negative-stain electron microscopy of inside-out FtsZ rings reconstituted on artificial membrane tubules show ribbons of protofilaments. *Biophys. J.* 103:59–68.
20. Arumugam, S., G. Chwastek, …, P. Schwille. 2012. Surface topology engineering of membranes for the mechanical investigation of the tubulin homologue FtsZ. *Angew. Chem. Int. Ed. Engl.* 51:11858–11862.
21. Lan, G., B. R. Daniels, …, S. X. Sun. 2009. Condensation of FtsZ filaments can drive bacterial cell division. *Proc. Natl. Acad. Sci. USA.* 106:121–126.
22. Loose, M., and T. J. Mitchison. 2014. The bacterial cell division proteins FtsA and FtsZ self-organize into dynamic cytoskeletal patterns. *Nat. Cell Biol.* 16:38–46.
23. Ramirez, D., D. A. García-Soriano, …, P. Schwille. 2016. Chiral vortex dynamics on membranes is an intrinsic property of FtsZ, driven by GTP hydrolysis. *bioRxiv.* https://doi.org/10.1101/079533.
24. Erickson, H. P. 2009. Modeling the physics of FtsZ assembly and force generation. *Proc. Natl. Acad. Sci. USA.* 106:9238–9243.
25. Erickson, H. P., D. E. Anderson, and M. Osawa. 2010. FtsZ in bacterial cytokinesis: cytoskeleton and force generator all in one. *Microbiol. Mol. Biol. Rev.* 74:504–528.
26. Nogales, E., K. H. Downing, …, J. Löwe. 1998. Tubulin and FtsZ form a distinct family of GTPases. *Nat. Struct. Biol.* 5:451–458.
27. Elsen, N. L., J. Lu, …, K. J. Lumb. 2012. Mechanism of action of the cell-division inhibitor PC190723: modulation of FtsZ assembly cooperativity. *J. Am. Chem. Soc.* 134:12342–12345.
28. Matsui, T., J. Yamane, …, I. Tanaka. 2012. Structural reorganization of the bacterial cell-division protein FtsZ from *Staphylococcus aureus*. *Acta Cryst. Sect. D Biol. Crystallography.* 68:1175–1188.
29. Ramírez-Aportela, E., J. R. López-Blanco, …, P. Chacón. 2014. Understanding nucleotide-regulated FtsZ filament dynamics and the monomer assembly switch with large-scale atomistic simulations. *Biophys. J.* 107:2164–2176.
30. Li, Y., J. Hsin, …, S. Ye. 2013. FtsZ protofilaments use a hinge-opening mechanism for constrictive force generation. *Science.* 341:392–395.
31. Huecas, S., O. Llorca, …, J. M. Andreu. 2008. Energetics and geometry of FtsZ polymers: nucleated self-assembly of single protofilaments. *Biophys. J.* 94:1796–1806.
32. Artola, M., L. B. Ruíz-Avila, …, S. Huecas. 2017. The structural assembly switch of cell division protein FtsZ probed with fluorescent allosteric inhibitors. *Chem. Sci. (Camb.).* 8:1525–1534.
33. Wagstaff, J. M., M. Tsim, …, J. Löwe. 2017. A polymerisation-associated conformational switch in FtsZ. *MBio.* 8, e00254–e00217.
34. Haydon, D. J., J. M. Bennett, …, L. Czaplewski. 2010. Creating an antibacterial with in vivo efficacy: synthesis and characterization of potent inhibitors of the bacterial cell division protein FtsZ with improved pharmaceutical properties. *J. Med. Chem.* 53:3927–3936.
35. Andreu, J. M., C. Schaffner-Barbero, …, A. J. Martín-Galiano. 2010. The antibacterial cell division inhibitor PC190723 is an FtsZ polymer-stabilizing agent that induces filament assembly and condensation. *J. Biol. Chem.* 285:14239–14246.
36. Buske, P. J., and P. A. Levin. 2012. Extreme C terminus of bacterial cytoskeletal protein FtsZ plays fundamental role in assembly independent of modulatory proteins. *J. Biol. Chem.* 287:10945–10957.
37. Gardner, K. A. J., D. A. Moore, and H. P. Erickson. 2013. The C-terminal linker of *Escherichia coli* FtsZ functions as an intrinsically disordered peptide. *Mol. Microbiol.* 89:264–275.
38. Buske, P. J., A. Mittal, …, P. A. Levin. 2015. An intrinsically disordered linker plays a critical role in bacterial cell division. *Semin. Cell Dev. Biol.* 37:3–10.
39. Sundararajan, K., A. Miguel, …, E. D. Goley. 2015. The bacterial tubulin FtsZ requires its intrinsically disordered linker to direct robust cell wall construction. *Nat. Commun.* 6:7281.
40. Marcelo, F., S. Huecas, …, J. M. Andreu. 2013. Interactions of bacterial cell division protein FtsZ with C8-substituted guanine nucleotide inhibitors. A combined NMR, biochemical and molecular modeling perspective. *J. Am. Chem. Soc.* 135:16418–16428.
41. Rivas, G., A. López, …, J. M. Andreu. 2000. Magnesium-induced linear self-association of the FtsZ bacterial cell division protein monomer. The primary steps for FtsZ assembly. *J. Biol. Chem.* 275:11740–11749.
42. Huecas, S., and J. M. Andreu. 2003. Energetics of the cooperative assembly of cell division protein FtsZ and the nucleotide hydrolysis switch. *J. Biol. Chem.* 278:46146–46154.
43. Cordeiro, T. N., F. Herranz-Trillo, …, P. Bernadó. 2017. Small-angle scattering studies of intrinsically disordered proteins and their complexes. *Curr. Opin. Struct. Biol.* 42:15–23.
44. Löwe, J., and L. A. Amos. 1999. Tubulin-like protofilaments in Ca^{2+}-induced FtsZ sheets. *EMBO J.* 18:2364–2371.
45. Ruiz-Avila, L. B., S. Huecas, …, J. M. Andreu. 2013. Synthetic inhibitors of bacterial cell division targeting the GTP-binding site of FtsZ. *ACS Chem. Biol.* 8:2072–2083.

46. Kuchibhatla, A., A. S. Abdul Rasheed, …, D. Panda. 2009. An analysis of FtsZ assembly using small angle x-ray scattering and electron microscopy. *Langmuir.* 25:3775–3785.
47. Glatter, O., and O. Kratky. 1982. Small Angle X-Ray Scattering. Academic Press, London, United Kingdom.
48. Díaz, J. F., E. Pantos, …, J. M. Andreu. 1994. Solution structure of GDP-tubulin double rings to 3 nm resolution and comparison with microtubules. *J. Mol. Biol.* 238:214–225.
49. Buske, P. J., and P. A. Levin. 2013. A flexible C-terminal linker is required for proper FtsZ assembly in vitro and cytokinetic ring formation in vivo. *Mol. Microbiol.* 89:249–263.
50. Turner, D. J., I. Portman, …, M. S. Turner. 2012. The mechanics of FtsZ fibers. *Biophys. J.* 102:731–738.
51. Wang, X., J. Huang, …, J. Lutkenhaus. 1997. Analysis of the interaction of FtsZ with itself, GTP, and FtsA. *J. Bacteriol.* 179:5551–5559.
52. Martin, T. G., T. A. Bharat, …, S. H. Scheres. 2016. Design of a molecular support for cryo-EM structure determination. *Proc. Natl. Acad. Sci. USA.* 113:E7456–E7463.
53. Frigon, R. P., and S. N. Timasheff. 1975. Magnesium-induced self-association of calf brain tubulin. I. Stoichiometry. *Biochemistry.* 14:4559–4566.
54. Lu, C., M. Reedy, and H. P. Erickson. 2000. Straight and curved conformations of FtsZ are regulated by GTP hydrolysis. *J. Bacteriol.* 182:164–170.
55. Huecas, S., and J. M. Andreu. 2004. Polymerization of nucleotide-free, GDP- and GTP-bound cell division protein FtsZ: GDP makes the difference. *FEBS Lett.* 569:43–48.
56. Hou, S., S. A. Wieczorek, …, P. Garstecki. 2012. Characterization of *Caulobacter crescentus* FtsZ protein using dynamic light scattering. *J. Biol. Chem.* 287:23878–23886.
57. Stark, H. 2010. GraFix: stabilization of fragile macromolecular complexes for single particle cryo-EM. *Methods Enzymol.* 481:109–126.
58. González, J. M., M. Vélez, …, G. Rivas. 2005. Cooperative behavior of *Escherichia coli* cell-division protein FtsZ assembly involves the preferential cyclization of long single-stranded fibrils. *Proc. Natl. Acad. Sci. USA.* 102:1895–1900.
59. Monterroso, B., G. Rivas, and A. P. Minton. 2012. An equilibrium model for the Mg^{2+}-linked self-assembly of FtsZ in the presence of GTP or a GTP analogue. *Biochemistry.* 51:6108–6113.
60. Ahijado-Guzmán, R., C. Alfonso, …, G. Rivas. 2013. Control by potassium of the size distribution of *Escherichia coli* FtsZ polymers is independent of GTPase activity. *J. Biol. Chem.* 288:27358–27365.
61. Monterroso, B., R. Ahijado-Guzmán, …, G. Rivas. 2012. Mg^{2+}-linked self-assembly of FtsZ in the presence of GTP or a GTP analogue involves the concerted formation of a narrow size distribution of oligomeric species. *Biochemistry.* 51:4541–4550.
62. Mingorance, J., M. Tadros, …, M. Vélez. 2005. Visualization of single *Escherichia coli* FtsZ filament dynamics with atomic force microscopy. *J. Biol. Chem.* 280:20909–20914.
63. Mateos-Gil, P., A. Paez, …, M. Vélez. 2012. Depolymerization dynamics of individual filaments of bacterial cytoskeletal protein FtsZ. *Proc. Natl. Acad. Sci. USA.* 109:8133–8138.
64. Hamon, L., D. Panda, …, D. Pastré. 2009. Mica surface promotes the assembly of cytoskeletal proteins. *Langmuir.* 25:3331–3335.
65. Erickson, H. P., D. W. Taylor, …, D. Bramhill. 1996. Bacterial cell division protein FtsZ assembles into protofilament sheets and mini-rings, structural homologs of tubulin polymers. *Proc. Natl. Acad. Sci. USA.* 93:519–523.
66. Chen, Y., H. Huang, …, H. P. Erickson. 2017. ZipA and FtsA* stabilize FtsZ-GDP miniring structures. *Sci. Rep.* 7:3650.
67. Oliva, M. A., S. C. Cordell, and J. Löwe. 2004. Structural insights into FtsZ protofilament formation. *Nat. Struct. Mol. Biol.* 11:1243–1250.
68. Srinivasan, R., M. Mishra, …, M. K. Balasubramanian. 2008. The bacterial cell division protein FtsZ assembles into cytoplasmic rings in fission yeast. *Genes Dev.* 22:1741–1746.
69. Mandelkow, E. M., E. Mandelkow, and R. A. Milligan. 1991. Microtubule dynamics and microtubule caps: a time-resolved cryo-electron microscopy study. *J. Cell Biol.* 114:977–991.
70. Buey, R. M., J. F. Díaz, and J. M. Andreu. 2006. The nucleotide switch of tubulin and microtubule assembly: a polymerization-driven structural change. *Biochemistry.* 45:5933–5938.
71. Brouhard, G. J., and L. M. Rice. 2014. The contribution of $\alpha\beta$-tubulin curvature to microtubule dynamics. *J. Cell Biol.* 207:323–334.
72. Osawa, M., and H. P. Erickson. 2013. Liposome division by a simple bacterial division machinery. *Proc. Natl. Acad. Sci. USA.* 110:11000–11004.
73. Housman, M., S. L. Milam, …, H. P. Erickson. 2016. FtsZ protofilament curvature is the opposite of tubulin rings. *Biochemistry.* 55:4085–4091.
74. Oliva, M. A., S. Huecas, …, J. M. Andreu. 2003. Assembly of archaeal cell division protein FtsZ and a GTPase-inactive mutant into double-stranded filaments. *J. Biol. Chem.* 278:33562–33570.
75. Yao, Q., A. I. Jewett, …, G. J. Jensen. 2017. Short FtsZ filaments can drive asymmetric cell envelope constriction at the onset of bacterial cytokinesis. *EMBO J.* 36:1577–1589.
76. Yang, X., Z. Lyu, …, J. Xiao. 2017. GTPase activity-coupled treadmilling of the bacterial tubulin FtsZ organizes septal cell wall synthesis. *Science.* 355:744–747.
77. Bisson-Filho, A. W., Y. P. Hsu, …, E. C. Garner. 2017. Treadmilling by FtsZ filaments drives peptidoglycan synthesis and bacterial cell division. *Science.* 355:739–743.
78. Denk, J., L. Huber, …, E. Frey. 2016. Active curved polymers form vortex patterns on membranes. *Phys. Rev. Lett.* 116:178301.
79. Coltharp, C., and J. Xiao. 2017. Beyond force generation: why is a dynamic ring of FtsZ polymers essential for bacterial cytokinesis? *BioEssays.* 39:1–11.

Biophysical Journal, Volume *113*

Supplemental Information

Self-Organization of FtsZ Polymers in Solution Reveals Spacer Role of the Disordered C-Terminal Tail

Sonia Huecas, Erney Ramírez-Aportela, Albert Vergoñós, Rafael Núñez-Ramírez, Oscar Llorca, J. Fernando Díaz, David Juan-Rodríguez, María A. Oliva, Patricia Castellen, and José M. Andreu

SUPPLEMENTAL INFORMATION

Self-organization of FtsZ polymers in solution reveals spacer role of the disordered C-terminal tail

S. Huecas, E. Ramírez-Aportela, A.Vergoñós, R. Nuñez-Ramírez, O. Llorca, J.F. Díaz, D. Juan-Rodríguez, M.A. Oliva, P. Castellen, J.M. Andreu

MATERIALS AND METHODS

FtsZ proteins

Full-length untagged FtsZ from *B. subtilis* (BsFtsZ) was overexpressed in *E. coli* C41(DE3) cells and purified by ammonium sulfate precipitation, ion exchange and hydrophobic chromatography, with ~0.05 guanine nucleotide bound per FtsZ (1). Untagged truncated BsFtsZ(1-318) (BsFtsZ-ΔCt) was obtained from a pHis17 plasmid in which a truncated version of the *ftsZ* gene (2) (from 1 to 954 bp, plus a TAA stop codon) was cloned into the NdeI/BamHI sites. BsFtsZ-ΔCt was purified similarly to the full length protein, except precipitation with 60% ammonium sulfate. His-tagged versions of full-length Bs-FtsZ and truncated BsFtsZ(1-315) were obtained through the expression from pAB20 and pAT19 plasmids respectively. The pAB20 plasmid (3) has an *ftsZ* copy from *B. subtilis* integrated in pET28a vector (Novagen) at *Nhe*I and *Not*I sites and it was used to generate pAT19 by the insertion of a stop codon at the I316 position. The *ftsZ* gene constructs were confirmed by complete open reading frame sequencing. The His-tagged proteins were overexpressed in *E. coli* BL21(DE3) and purified using Ni-affinity chromatography in 50mM Tris-HCl, 50 mM KCl, 10% glycerol, pH 8.0, with an imidazole gradient (50mM to 1M). His-tags were cleaved with thrombin yielding proteins GSHMAS-BsFtsZ (tag-BsFtsZ) and GSHMAS-BsFtsZ(1-315) (tag-BsFtsZ-ΔCt) respectively. The N-terminal residues were confirmed by Edman sequencing purified tag-BsFtsZ-ΔCt with an Applied Biosystems Procise 494 sequencer. Two additional chromatographic steps were used: anion exchange (HiTrapQ HP) in 50 mM Mes-KOH, 5 mM $MgCl_2$, 10% glycerol, pH 6.5, with a KCl gradient (50mM to 1M) and size exclusion (Superdex 75) in 50mM Tris-HCl, 50 mM KCl, 1 mM EDTA, 10% glycerol, pH 7.5. These proteins contained ~0.8 guanine nucleotide bound.

The C-terminal constructs BsFtsZ-ΔC17 (4), BsFtsZ-ΔCTL25, BsFtsZ-ΔCTL50, BsFtsZ-CTLA50, BsFtsZ-CTLA100 and BsFtsZ CTLA249 (5) were expressed from their corresponding plasmids (Table S1), kindly provided by the authors, in C41(DE3) cells and purified as native untagged BsFtsZ, with minor modifications. BsFtsZ-ΔC17 and BsFtsZ-ΔCTL25 were precipitated with 45% ammonium sulfate, BsFtsZ-ΔCTL50 with 65%, BsFtsZ-CTLA50 with 40%, BsFtsZ-CTLA100 and BsFtsZ-CTLA259 with 30% ammonium sulfate. These proteins contained 0.03 to 0.08 guanine nucleotide bound per FtsZ.

FtsZ from *E. coli* (EcFtsZ) was overproduced in transformed *E. coli* BL21(DE3) cells and purified by Ca^{2+}-precipitation and anion-exchange, with ~0.8 guanine nucleotide bound (6).

Thermophilic FtsZ from *M. jannaschii* (MjFtsZ) was overexpressed in *E. coli* BL21(DE3) pLyS cells, purified by ammonium sulfate precipitation, ion exchange and hydrophobic chromatography, containing ~0.45 guanine nucleotide bound (7).

Polymerization conditions

BsFtsZ assembly experiments were performed in 50 mM Tris-HCl, 50 mM KCl, 1 mM EDTA, 10 mM $MgCl_2$, pH 7.4 (Tris50 buffer), at 25 °C. Polymerization was started by addition of 0.1 mM GMPCPP or 1 mM GTP and it was monitored by right angle light scattering at 350 nm (0.5 nm band-pass) using a Fluromax-4 spectrofluorometer. Aliquots of the polymer solutions were adsorbed to carbon-coated grids, negatively stained with 2% uranyl acetate and examined with a Jeol 1230 electron microscope operated at 100 kV.

EcFtsZ assembly experiments were performed in 25 mM Pipes/KOH, 250mM KCl, 1 mM EDTA, 10 mM $MgCl_2$, pH 7.5 (Pipes250 buffer) at 25 °C, or in Tris50 buffer as above for comparison. Assembly was started by nucleotide addition: 0.1 mM GMPCPP, or 1 mM GTP, or a GTP (1mM) regenerating system consisting of 1 U/mL acetate kinase and 7.5 mM acetyl phosphate, or 1 mM GDP (negative control) or 0.1 mM GMPCP (negative control).

MjFtsZ was assembled in 50 mM Mes/KOH, 50 mM KCl, 1 mM EDTA, 10 mM $MgCl_2$, pH 6.5 (Mes50 buffer) at 55 °C, with 0.2 mM GMPCPP or 4 mM GTP

FtsZ polymer formation was measured by isothermal pelleting and protein concentration measurement (1). The Cr values of BsFtsZ and tag-BsFtsZ-ΔCt were 6.6 ± 1.0 μM and 1.6 ± 0.2 μM respectively with 2 mM GTP, 2.2 ± 0.4 μM and 1.0 ± 0.1 μM with 0.1 mM GMPCPP. Tag-BsFtsZ(1-382) assembled with Cr values similar to BsFtsZ (5.8 ± 1.4 μM with GTP and 1.5 ± 0.8 μM with GMPCPP).

Biochemical methods

The hydrolysis of GTP (2mM) or GMPCPP (0.1 mM) was measured from the released inorganic phosphate (1). The hydrolysis rate values given are referred to polymerized FtsZ, that is, total FtsZ concentration (10 to 20 µM) minus the Cr.

To determine nucleotide content in FtsZ polymers, nucleotides were extracted from FtsZ polymer pellets by the addition of $HClO_4$ (7) and analyzed employing an anion exchange column (VYDAC 3021C4.6, 10 µm, 4.6 mm x 250 mm) with a gradient of 25 mM NaH2PO4/Na2HPO4, pH 2.8 to 125 mM NaH2PO4/Na2HPO4, pH 2.9, detecting nucleotides by absorbance at 254 nm, with an AKTAPurifier system (GE Healthcare).

Sedimentation velocity experiments with unpolymerized FtsZ were made employing a Beckman XLI analytical ultracentrifuge with the interference optics (8) and analyzed with SEDFIT (9). Sedimentation coefficients of FtsZ ring models were calculated with HYDRO++ (10) using the BsFtsZ monomers sedimentation coefficient, with HYDROPRO (11) from SaFtsZ atomic model coordinates, and with HYDROMIC (12) from the electron microscopy volume of EcFtsZ rings.

SAXS experiments

Time-resolved small angle synchrotron X-ray solution scattering measurements of FtsZ and its polymers were performed at the ALBA BL11-NCD beam line. The camera length was 2.1 m and the X-ray energy 10 keV (λ = 1.24 Å). An ADSC Quantum 210r CCD detector (210 x 210 mm^2; 4096 x 4096 pixel) was employed, with a 6 mm centered beam stop, which provided a useful range of q = 0.01 to 0.22 $Å^{-1}$. The scattering vector modulus q is defined as $q = 4\pi (\sin \theta) / \lambda$, where 2θ is the angle of incident to scattered radiation and λ the X-ray wavelength. The q values were calibrated using the diffraction maxima of silver behenate. Preliminary SAXS data were acquired at former ESRF Spanish BM16 with a similar q-range. Comparative static measurements of truncated BsFtsZ-ΔCt and full length BsFtsZ were subsequently made at the ESRF BM29-BioSAXS beam line using the capillary sample changer robot and Pilatus 1M detector.

A vertical thermostated sample cell with mica windows and an optical path of 3 mm was employed at ALBA BL11-NCD. The degassed samples (180 µL) were loaded from the bottom with protein electrophoresis pipette tips (BioRad # 223-9915), which were introduced through a channel at the top, avoiding bubble formation. The X-ray beam size was approximately 600 μm (horizontal) x 138 μm (vertical). The protein solution was scanned, irradiating during 0.5 s, each 15 s, in a series of 63 non-overlapping evenly spaced positions within a 3mm (horizontal) x 7 mm (vertical) area, by automatically controlling the position of the sample stage and the shutter. This procedure avoided radiation damage. The dead time between sample loading and the first measurement was ~2 min.

The X-ray scattering data were integrated with the FIT2D software (http://www.esrf.eu/computing/scientific/FIT2D/), normalized for the incident intensity, processed with PRIMUS (13) and analyzed with GMOM (14). For each protein sample, the scattering by a carefully matched buffer reference was subtracted from the data. The time-resolved data were subtracted frame by frame, employing a PerL script (E.R.A., unpublished).

The instrumental set-up was tested measuring the scattering profile of delipidated bovine serum albumin (BSA, Sigma; 4.3, 2,2 and 1.1 g/L in Tris50 buffer, which afforded a radius of gyration value $R_G = 27.0 \pm 1.5$ Å and was superimposable within experimental error to a standard scattering profile of BSA from the Small Angle Scattering Biological Data Bank (SASBDB; entry SASDA32, 25.6 g/L BSA in 50 mM Hepes, 50 mM KCl; $R_G = 29$ Å). To test the instrument performance with large protein assemblies, we measured the scattering profile of microtubules assembled from tubulin (120 μM) with docetaxel (130 μM) in 10 mM sodium phosphate buffer, 6 mM $MgCl_2$, 1 mM GTP, pH 6.7, at 37 °C. The position of the scattering maxima (q, Å^{-1}) was very close to our reference values (15): J_{01}, 0.029 (ref. 0.031); J_{02}, 0.056 (ref. 0.057); J_{03}, 0.086 (ref. 0.086); J_n, 0.118 (ref. 0.121); J_3, 0.159 (ref. 0.160); J_{n-3}, 0.179 (ref. 0.177).

X-ray scattering by FtsZ polymer models

FtsZ polymer models were constructed FilaSitus program (http://situs.biomachina.org/fila/; (16)), employing the filament crystal structure of *Staphylococcus aureus* FtsZ (SaFtsZ; PDB entry 3vo8). Theoretical scattering curves were generated with CRYSOL (https://www.embl-hamburg.de/biosaxs/crysol.html, (17)). Default parameters were used with the following exceptions: maximum order of harmonics 30, order of Fibonacci grid 18, maximum q-value 0.30 and number of points 256 (except ring models that were calculated with 1024 points).

Model analysis of X-ray scattering by FtsZ single filaments. For convenience in this detailed description of model analysis, we will focus first on single filaments (Figure 4) and the higher angle scattering and then proceed to multiple filaments (Figure 2B) and lower angle scattering features. We constructed single filaments made of 140 FtsZ monomers with different curvature angles between consecutive monomers of 0° (straight, 6160 Å long), 0.5, 1, 1.5, 2 and 2.57° (a closed 1960 Å diameter ring) (Fig. S2). The direction of curvature employed is similar to that of SaFtsZ-GTP filaments in molecular dynamics simulations, which leaves the FtsZ C-terminal end on the outside, and the curvature angles are within the range observed (18). The straight model has a sharp peak at $q = 0.143$ Å^{-1}, corresponding to the 44 Å spacing between subunits along the filament. However, this peak could hardly be appreciated in the experimental SAXS profiles, except in BsFtsZ-ΔCt (Figure 2A) and in the more concentrated EcFtsZ polymer samples (Figure 3). The 0.14 Å^{-1} peak disappears in the curved single filament models, but undulations appear in the higher angle region that have not been experimentally observed. These undulations are out of phase in the different models and tend to smooth out in linear combinations of SAXS profiles calculated for filaments with different degrees of curvature, thus simulating filament flexibility (Fig. S2, dark grey line). As the filaments curve beyond a semi-circle and approach ring closure, a series of periodic ripples evenly spaced each ~0.003 Å^{-1} appear throughout the model scattering profile. These ripples correspond to the subsidiary maxima of a J_0-like Bessel function arising from rings with mean diameter ~2000 Å and their spacing is inversely proportional to the ring diameter (19). Combining rings of close sizes (100, 120 and 140 monomers) hardly smoothed the model ripples (Fig. S2, light grey line); notice that these features are absent from the experimental data (Figures 2 - 3). Mini-rings made of 16 monomers (224 Å diameter) give a sinusoidal pattern with a longer period (~0.03 Å^{-1}). Reversing the direction of curvature to have the FtsZ C-terminal end on the inside of the mini-rings (as in tubulin protofilaments peeling outwards from disassembling microtubule ends) does not change their scattering profile at our resolution. Combining mini-rings of close sizes (14, 16 and 18 monomers) smoothed the model scattering profile in the middle region but left periodic features in the low and high angle zones (Fig. S2) that have not been experimentally observed.

The effects of varying the filament length were examined with increasing number of monomers at two different curvature angles (Fig. S3). The ~0.14 Å^{-1} maximum is more marked in models covering circular arches up to 80° and disappears in the longer models, which show undulations and ripples as above. However, the higher angle undulations smooth by combining filaments of close sizes (100, 120 and 140 monomers) with 1° curvature angle between consecutive monomers; similarly combining filaments (40, 60 and 80 monomers) with 3.5° curvature angle cancels the ripples along the profile (Fig. S3, grey lines), and certain individual S-shape models lack ripples (Fig. S3, models *m* and *n*). Thus, single filament models of variable curvature and length (Figs. S2 and S3), rather than rings of close sizes or straight filaments, are qualitatively compatible with the smooth higher angle zone of the experimental EcFtsZ and BsFtsZ polymer SAXS.

In order to more closely modeling X-ray scattering by FtsZ polymer solutions it has to be taken into account that these always contain a concentration of unassembled protein, the critical protein concentration (Cr) required for assembly, which depends on the FtsZ species and solution conditions (20, 21). We thus simulated the Cr effects on SAXS with linear combinations of the model filaments scattering curves (Fig. S2 and S3) with a small proportion (5%; exp. value Cr = 0.088 g/L) of the scattering by a similar number of unassembled FtsZ monomers. This procedure softens the 0.14 $Å^{-1}$ maximum of straight models and the higher angle undulations of curved models, making their corresponding model mixture qualitatively compatible with the EcFtsZ polymers experimental data (see Figure 3); however, this is clearly not the case for ring model mixtures, in which characteristic sinusoidal oscillations remain at low and mid angles after mixing with unassembled FtsZ monomers. The amplitude of these oscillations clearly exceeds experimental noise: for example, the oscillations of ring model mixture scattering intensity at 0.12 $Å^{-1}$ have relative amplitude (± 26%) five times larger than the normalized standard deviation (5 %) of the scattering by the concentrated EcFtsZ sample (Figure 3). Taking into account that FtsZ filaments were not crystal-straight during molecular dynamics simulations (18) or in cryo-EM (20, 22), we concluded from the model analysis that the smooth higher angle zone of the experimental EcFtsZ polymers SAXS is compatible with single filament FtsZ models of variable curvature and length. Such ensemble of FtsZ filament configurations may include S-shapes, as the model shown in Figure 3, as well as less curved S- and C-shapes, and a proportion of multiple filaments (analyzed below) should not be excluded. However, a polymer population consisting of rings of close sizes (100-120-140 monomers) appears incompatible with the EcFtsZ SAXS data; we cannot rule out annealed filament tangles of this size. Mini-ring models (14-16-18 monomers) are also inconsistent with the data (Figure 3). However, a 20% of FtsZ forming mini-rings and 80% in curved filaments would be qualitatively compatible with the EcFtsZ SAXS data.

Model analysis of X-ray scattering by FtsZ filament bundles.

We next constructed multiple filament models, in order to capture the ~0.09 $Å^{-1}$ and ~0.05 $Å^{-1}$ maxima of the BsFtsZ experimental profiles (Figure 2A). For simplicity, we first analyze straight filaments and the ~0.09 $Å^{-1}$ maximum and then proceeded to multiple curved filaments and the ~0.05 $Å^{-1}$ maximum. Two parallel filaments with a 70 Å center to center distance reproduce the 0.09 Å^{-1} maximum (Figure S4, models i and j). Importantly, these model filaments do not touch each other, and touching filaments do not give rise to this maximum (Figure S4, models f, g, h; 48 Å center to center distance). A sharp monomer repeat peak at 0.14 Å^{-1} appears in straight models (c, d, e, i) that is modulated into a characteristic bulge by shifting one filament with respect to the other by half a monomer length (compare models i and j). Rotating the in-phase filaments by 90° and making them closer (38 Å center to center) slightly softened this peak, whereas performing the same operation with the shifted filament pair gave a different, wider maximum centered around 0.17 Å^{-1} (not shown). Of note, the ~0.15 Å^{-1} bulge in multiple filament models resembles the 0.14 Å^{-1} experimental feature of truncated BsFtsZ-ΔCt (Figure 2A), which lacks the 0.09 Å^{-1} maximum as the touching filaments models (Figure S4, model f). This 0.09 Å^{-1} maximum becomes prominent in non-touching filament ribbons upon increasing the number of strands (models i, k, l).

Nevertheless, straight models hardly reproduce the 0.05 Å^{-1} maximum, which corresponds to a 126 Å characteristic distance between filaments. This feature is better captured by triple curved filaments (Figure S5, models a-d). Three concentric filaments, made of 65-60-55 subunits each, radially spaced 70 Å display both an scattering maximum at 0.09 Å^{-1} and a shoulder at 0.05 Å^{-1} (model *a*). But they also have a prominent minimum at 0.15 Å^{-1} and peak at 0.18 Å^{-1} that are absent from the data; these unwanted model features can be suppressed by introducing some disorder, which we simulated by displacing one (models *b* and *c*) or two of the filaments (model *d*) by 36 Å perpendicularly to the curvature plane, and readjusting to 70 Å the distance between neighbor filaments. Model *d*, or a combination of models, resemble better the ~0.05 Å^{-1} and ~0.09 Å^{-1} maxima together with the smooth higher angle scattering by BsFtsZ polymers. It is conceivable that bundles of more than three curved, 70 Å -spaced filaments, can also reproduce the SAXS features. However, circularly closed triple ring models (Figure S5, models e-h; mean diameter 1470 Å) or their combination showed the periodic maxima typical of rings, now modulated by inter-ring interference, which are absent from the experimental profiles. Three stacked rings models or an equivalent flat helix show reinforced ring maxima (Figure S5, model i).

Combining FtsZ triple filament models with a 5% of unassembled monomers as before (BsFtsZ experimental Cr = 0.076 g/L), we found that triple curved filaments reproduce the 0.05 and 0.09 Å^{-1} scattering maxima and smooth higher angle region of the BsFtsZ-GMPCPP polymer solutions. These models are exemplified in Figure 2B by an off-plane triple curved filament, which is made of 65 + 60 + 55 crystallographic FtsZ monomers and has an end-to-end distance of 1430 Å (note that length should actually be variable). Straight triple filaments resemble less well the BsFtsZ experimental data whereas the triple ring models generate ripples that are absent from the data. The lower angle scattering ($q = 0.01$ to ~ 0.02 $Å^{-1}$) by the models is not as steep as in BsFtsZ-GMPCPP polymers, which indicates that the later are still larger scattering objects, as indicated by their turbidity in white light. We suggest that they form by aggregation or annealing of curved filaments bundles similar to those described by the models. We conclude from this model analysis that the experimental BsFtsZ–GMPCPP polymer SAXS can be explained by loose bundles of ≥ 3 curved protofilaments of variable length, laterally spaced 70 Å, and their aggregates. We found straight filament bundles less likely and ordered circularly closed FtsZ rings incompatible with the SAXS profiles of BsFtsZ. In contrast, the distinct scattering by the polymers of tail-less BsFtsZ-ΔCt-GMPCPP can be explained by straight tight bundles of ≥ 2 protofilaments, which is exemplified by a triple filament in Figure 2B.

Scheme of a FtsZ bundle with C-terminal tails

The C-terminal tails connecting protofilaments were constructed as follows. The last 15 C-terminal amino acid residues of SaFtsZ were initially predicted with the I-Tasser server (23) to form a helical structure. Subsequently, potential binding sites for this segment in the FtsZ subunit of the contiguous filament were searched using the Frodock 2.0 server (24), and one of the 10 best solutions was selected. The rest of the peptide chain linking to the FtsZ core was completed using the loops generation RCD+ server (25). Several C-tails were then re-configured for Fig. 6, and the protein electrostatic contact potential displayed with PyMOL.

Cryo-electron microscopy

Samples were applied to holey carbon grids (Quantifoil) after glow-discharge and immediately blotted and vitrified using a GATAN or FEI Vitrobot cryo-plunger. Micrographs were taken at x40000 nominal magnification in a Jeol 1230 electron microscope operated at 100 kV and equipped with a Gatan liquid nitrogen specimen holder for cryo-EM. Cryo-EM images were taken from the hole areas, where the ice lacks any supporting film underneath, under low dose conditions and different defocus, with a CMOS Tvips TemCam-F416 camera, at 2.84 Å per pixel. Image-J software was used for filament thickness measurements and diffractogram calculations. Mini-ring images were picked and subsequently aligned and classified using SCIPION package (http://scipion.cnb.csic.es; (26)).

SUPPLEMENTAL REFERENCES

1. Ruiz-Avila, L. B., S. Huecas, M. Artola, A. Vergonos, E. Ramirez-Aportela, E. Cercenado, I. Barasoain, H. Vazquez-Villa, M. Martin-Fontecha, P. Chacon, M. L. Lopez-Rodriguez, and J. M. Andreu. 2013. Synthetic Inhibitors of Bacterial Cell Division Targeting the GTP-Binding Site of FtsZ. ACS Chem. Biol. 8:2072-2083.
2. Oliva, M. A., D. Trambaiolo, and J. Lowe. 2007. Structural insights into the conformational variability of FtsZ. J. Mol. Biol. 373:1229-1242.
3. Blasios, V., A. W. Bisson, P. Castellen, M. L. C. Nogueira, J. Bettini, R. V. Portugal, A. C. M. Zeri, and F. J. Gueiros. 2013. Genetic and Biochemical Characterization of the MinC-FtsZ Interaction in Bacillus subtilis. Plos One 8:12.
4. Buske, P. J., and P. A. Levin. 2012. Extreme C Terminus of Bacterial Cytoskeletal Protein FtsZ Plays Fundamental Role in Assembly Independent of Modulatory Proteins. J. Biol. Chem. 287:10945-10957.
5. Buske, P. J., and P. A. Levin. 2013. A flexible C-terminal linker is required for proper FtsZ assembly in vitro and cytokinetic ring formation in vivo. Mol. Microbiol. 89:249-263.
6. Rivas, G., A. Lopez, J. Mingorance, M. J. Ferrandiz, S. Zorrilla, A. P. Minton, M. Vicente, and J. M. Andreu. 2000. Magnesium-induced linear self-association of the FtsZ bacterial cell division protein monomer - The primary steps for FtsZ assembly. J. Biol. Chem. 275:11740-11749.
7. Huecas, S., and J. M. Andreu. 2003. Energetics of the cooperative assembly of cell division protein FtsZ and the nucleotide hydrolysis switch. J. Biol. Chem. 278:46146-46154.
8. Marcelo, F., S. Huecas, L. B. Ruiz-Avila, F. J. Canada, A. Perona, A. Poveda, S. Martin-Santamaria, A. Morreale, J. Jimenez-Barbero, and J. M. Andreu. 2013. Interactions of Bacterial Cell Division Protein FtsZ with C8-Substituted Guanine Nucleotide Inhibitors. A Combined NMR, Biochemical and Molecular Modeling Perspective. J. Am. Chem. Soc. 135:16418-16428.
9. Schuck, P. 2000. Size-distribution analysis of macromolecules by sedimentation velocity ultracentrifugation and Lamm equation modeling. Biophys. J. 78:1606-1619.
10. Garcia de la Torre, J., G. del Rio Echenique, and A. Ortega. 2007. Improved calculation of rotational diffusion and intrinsic viscosity of bead models for macromolecules and nanoparticles. J. Phys. Chem. B 111:955-961.
11. Ortega, A., D. Amoros, and J. Garcia de la Torre. 2011. Prediction of Hydrodynamic and Other Solution Properties of Rigid Proteins from Atomic- and Residue-Level Models. Biophys. J. 101:892-898.
12. Garcia de la Torre, J. G., O. Llorca, J. L. Carrascosa, and J. M. Valpuesta. 2001. HYDROMIC: prediction of hydrodynamic properties of rigid macromolecular structures obtained from electron microscopy images. European Biophysics Journal with Biophysics Letters 30:457-462.
13. Konarev, P. V., V. V. Volkov, A. V. Sokolova, M. H. J. Koch, and D. I. Svergun. 2003. PRIMUS: a Windows PC-based system for small-angle scattering data analysis. J. Appl. Crystallogr. 36:1277-1282.
14. Svergun, D. I. 1992. Determination of the regularization parameter in indirect-transform methods using perceptuial criteria. J. Appl. Crystallogr. 25:495-503.
15. Andreu, J. M., J. F. Diaz, R. Gil, J. M. Depereda, M. G. Delacoba, V. Peyrot, C. Briand, E. Townsandrews, and J. Bordas. 1994. Solution structure of taxotere-induced microtubules to 3 nm resolution. J. Biol. Chem. 269:31785-31792.
16. Wriggers, W. 2012. Conventions and workflows for using Situs. Acta Crystallographica Section D-Biological Crystallography 68:344-351.
17. Svergun, D., C. Barberato, and M. H. J. Koch. 1995. CRYSOL - A program to evaluate x-ray solution scattering of biological macromolecules from atomic coordinates. J. Appl. Crystallogr. 28:768-773.

18. Ramirez-Aportela, E., J. R. Lopez-Blanco, J. M. Andreu, and P. Chacon. 2014. Understanding Nucleotide-Regulated FtsZ Filament Dynamics and the Monomer Assembly Switch with Large-Scale Atomistic Simulations. Biophys. J. 107:2164-2176.
19. Diaz, J. F., E. Pantos, J. Bordas, and J. M. Andreu. 1994. Solution structure of GDP-tubulin double rings to 3 nm resolution and comparison with microtubules. J. Mol. Biol. 238:214-223.
20. Huecas, S., O. Llorca, J. Boskovic, J. Martin-Benito, J. M. Valpuesta, and J. M. Andreu. 2008. Energetics and geometry of FtsZ polymers: Nucleated self-assembly of single protofilaments. Biophys. J. 94:1796-1806.
21. Andreu, J. M., C. Schaffner-Barbero, S. Huecas, D. Alonso, M. L. Lopez-Rodriguez, L. B. Ruiz-Avila, R. Nunez-Ramirez, O. Llorca, and A. J. Martin-Galiano. 2010. The antibacterial cell division inhibitor PC190723 is a FtsZ polymer stabilizing agent which induces filament assembly and condensation. J. Biol. Chem., 285,14239-14246.
22. Turner, D. J., I. Portman, T. R. Dafforn, A. Rodger, D. I. Roper, C. J. Smith, and M. S. Turner. 2012. The Mechanics of FtsZ Fibers. Biophys. J. 102:731-738.
23. Yang, J., R. Yan, A. Roy, D. Xu, J. Poisson, and Y. Zhang. 2015. The I-TASSER Suite: Protein structure and function prediction. Nat. Methods 12:7-8.
24. Ramírez Aportela, E., J. R. López-Blanco, and P. Chacón. 2016. FRODOCK 2.0: Fast Protein-Protein docking server. Bioinformatics 32:2386-2388.
25. López-Blanco, J. R., A. J. Canosa-Valls, Y. Li, and P. Chacón. 2016. RCD+: Fast loop modeling server. Nucleic Acids Res. 44:W395-400.
26. de la Rosa-Trevin, J. M., A. Quintana, L. del Cano, A. Zaldivar, I. Foche, J. Gutierrez, J. Gomez-Blanco, J. Burguet-Castell, J. Cuenca-Alba, V. Abrishami, J. Vargas, J. Oton, G. Sharov, J. L. Vilas, J. Navas, P. Conesa, M. Kazemi, R. Marabini, C. O. S. Sorzano, and J. M. Carazo. 2016. Scipion: A software framework toward integration, reproducibility and validation in 3D electron microscopy. Journal of Structural Biology 195:93-99.
27. Frigon, R. P., and S. N. Timasheff. 1975. Magnesium-induced self-association of calf brain tubulin: stoichiometry. Biochemistry 14:4559-4566.

Table S1: FtsZ proteins and expression plasmids employed in this work

Protein name	**Protein sequence**	**Plasmid description**	**Reference**
BsFtsZ	Native BsFtsZ(1-382)	pHis17-ftsZ_{Bs}	1, 2
tag-BsFtsZ	GSHMAS-BsFtsZ(1-382)	pET28a(+)-ftsZ_{Bs} (pAB20)	3
BsFtsZ-ΔCt	BsFtsZ(1-318)	pHis17-$\mathit{ftsZ\Delta Ct}_{Bs}$	This study
tag- BsFtsZ-ΔCt	GSHMAS-BsFtsZ(1-315)	pET28a(+)-$\mathit{ftsZ\Delta Ct}_{Bs}$ (pAT19)	This study
BsFtsZ-ΔC17	BsFtsZ(1-365) (ΔCTC, ΔCTV)	pET21b(+)-$\mathit{ftsZ\Delta C17}_{Bs}$	4
BsFtsZ-ΔCTL25	BsFtsZ, deletion of the last 25 CTL residues	pET21b(+)-$\mathit{ftsZ\Delta CTL25}_{Bs}$	5
BsFtsZ-ΔCTL50	BsFtsZ, complete deletion of the CTL	pET21b(+)-$\mathit{ftsZ\Delta CTL50}_{Bs}$	5
BsFtsZ-CTLA50	BsFtsZ, native CTL replacement by residues 322-367 from *Agrobacterium tumefaciens* FtsZ	pET21b(+)-*ftsZCTLA50*	5
BsFtsZ-CTLA100	BsFtsZ, native CTL replacement by residues 322-417 from *A. tumefaciens* FtsZ	pET21b(+)-*ftsZCTLA100*	5
BsFtsZ-CTLA249	BsFtsZ, native CTL replacement by residues 322-566 from *A. tumefaciens* FtsZ	pET21b(+)-*ftsZCTLA249*	5
EcFtsZ	Native EcFtsZ	pET28a(+)-ftsZ_{Ec}	6
MjFtsZ	Native MjFtsZ	pHis17-ftsZ_{Mj}	7

SUPPLEMENTAL FIGURE LEGENDS

Figure S1. Effects of small molecule modulators of FtsZ polymer assembly. Related to main text and Figure 2. The scattering profiles of BsFtsZ (50 μM) assembled with GTP or GMPCPP, plus the polymer stabilizer PC190723 (60 μM) or the inhibitor UCM53 (60 μM) are shown as indicated. In each case, the grey tracing corresponds to a sample with nucleotide and no modulator, whereas the black points are from a parallel sample to which the modulator has been added.

Figure S2. X-ray scattering by FtsZ single filament models with varying curvature. Related to main text and Figure 4. Models were built with head-to-tail associated SaFtsZ monomers (indicated by the enlarged ribbon diagram: see Methods). Model **a** is a straight protofilament made of 140 monomers with 0° bending angle per monomer, model **b** with 0.5° angle, model **c** with 1° angle, model **d** with 1.5° angle, model **e** with 2° angle. The dark grey profile below is a linear combination of the scattering profiles of curved models b (30%), c (40%) and d (30%). Models **f, g** and **h** are closed rings made of 140 monomers (with 2.57° bending angle), 120 and 100 monomers respectively. The light grey profile is a combination of scattering by ring models f (30%), g (40%) and h (30%). Model **i, j, k** are small rings made of 14, 16 and 18 monomers (only model j is shown). The light grey dashed line is a combination of the scattering by ring models i (30%), j (40%) and k (30%). Each scattering profile is plotted using the same color as its corresponding model

Figure S3. X-ray scattering by FtsZ single curved filament models of varying length. Related to main text and Figure 4. Curved models were constructed with 1° and 3.5° bending angles between consecutive monomers. Models **a, b, c, d, e, f** and **g** (1° angle) are respectively made of 20, 40, 60, 80, 100, 120 and 140 monomers. Models **h, i, j, k and l** (3.5° angle) are respectively made of 20, 40, 60, 80 and 100 monomers. S-shape model **m** is built of 60 + 60 monomers with 3.5° and -3.5° bending angles. Model **n** is made of four 36 monomer sections with alternating 5° and -5° bending angles. Each calculated scattering profile is displayed in the same color as its model, with continuous (1°) or dash lines (3.5°, 5°). The continuous grey line is a combination of the scattering profile of model e (30%), f (40%) and g (30%). The dash grey line corresponds to a combination of models i (30%), j (40%) and k (30%).

Figure S4. X-ray scattering by FtsZ multiple straight filament models. Related to main text and Figure 2. Model **a** is a SaFtsZ monomer, models **b** are a straight crystallographic heptamer and a curved GTP-bound molecular dynamics heptamer (18). Models **c**, **d**, and **e** are straight single filaments respectively made of 100, 120 and 140 monomers. Model **f** is made of two touching 140-monomer filaments with a lateral center to center distance of 48 Å; models **g** and **h** are corresponding triple and quadruple filaments respectively; model **i** two non-contacting filaments with a 70 Å distance; model **j** is similar to model i but one of the filaments has been axially shifted by half a monomer distance. Models **k** and **l** are respectively triple and quadruple filaments built as model j.

Figure S5. X-ray scattering by FtsZ multiple curved filament models. Related to main text and Figure 2. Model **a,** shown in orthogonal and end views, consists of three concentric arcs made of 65-60-55 monomers each, radially spaced 70 Å (with curvature angles of 3.138°, 3.437° and 3.800°). In models **b** and **c** the central or one side ring has been displaced 36 Å away from the plane defined by the other two rings, and the distance between rings readjusted to 70 Å. In model **d** the central and one side rings have been similarly displaced from the plane of the other ring. The calculated scattering profiles are shown in the same colors as the models. The scattering profiles at the bottom part of the figure correspond to closed rings of the same dimensions (models **e-h**). The dashed blue line is the scattering profile of a stack of three 110 FtsZ monomer rings consecutively spaced 7 Å (model **i**, not shown). A flat helix with corresponding dimensions gave a very similar scattering profile. The grey line is a combination of the scattering profiles of model b (30%), model c (40%) and model d (30%). The light grey line at the bottom is an equivalent combination of closed ring models.

Figure S6. Electron micrographs of negatively stained BsFtsZ and BsFtsZ-ΔCt polymers. Related to Figure 4. 50 μM FtsZ was polymerized in Tris50 buffer with 10 mM $MgCl_2$ and 0.1 mM GMPCPP or 1 mM GTP at 25 °C and polymers formed were observed by EM. Bar, 2000 Å.

Figure S7. Cryo-EM of BsFtsZ, tag-BsFtsZ-ΔCt and tag-BsFtsZ polymers with GTP. Related to Figure 4. 50 μM BsFtsZ (**A**), tag-BsFtsZ-ΔCt (**B**) and tag-BsFtsZ (**C**) were assembled in Tris50 buffer with 10 mM $MgCl_2$ and 1 mM GTP at 25 °C, and polymers formed were visualized by cryo-EM; bar, 1000 Å; enlarged areas (bar, 500 Å) from each picture and their diffractogram are shown and some more examples of BsFtsZ are included to show spacing variability obtained from different areas (D). The distance between filaments in bundles of BsFtsZ (black bars; mean ± s.d.: 66.0 ± 7.5 Å (GTP); 70.5 ± 8.6 Å (GMPCPP)) and tag-BsFtsZ-ΔCt (gray bars; 55.2 ± 11.0 Å (GTP) 57.8 ± 13.2 Å (GMPCPP)) were measured and the distribution plotted (**D, E**). Notice that the spread of these distributions may partially result from inherent measurement errors.

Figure S8. Cryo-EM of disassembling BsFtsZ polymers. Related to main text. **(A)** light scattering time courses of 2 g/L BsFtsZ assembly in Tris50 buffer with 10 mM $MgCl_2$ and 0.1 mM GMPCPP or 1 mM GTP; nucleotides were added at time 0. Samples were taken at different stages during de-polymerization and observed by cryo-EM. BsFtsZ assembled with GMPCPP at 70-50% (**B**) and 20-5% (**C**) light scattering. **D,** BsFtsZ assembled with 0.1 mM GMPCP. **E**, BsFtsZ assembled with GTP at 50-30% (**E**) and 20-10% (**F**) light scattering. **G**, BsFtsZ assembled with 1 mM GDP. Bar, 1000 Å.

Figure S9. Cryo-EM of BsFtsZ C-terminal constructs polymers. Related to main text. BsFtsZ-ΔC17 (**A** and **B**), BsFtsZ-ΔCTL25 (**C** and **D**), BsFtsZ-ΔCTL50 (**E** and **F**) are described in main text. Each BsFtsZ construct (50 μM) was assembled in Tris50 buffer with 10 mM $MgCl_2$ and 0.1 mM GMPCPP at 25 ºC, in the absence (**A**, **C**, **E**) or presence of 20 μM PC190723 (**B**, **D**, **F**), and polymers formed were visualized by cryo-EM. Bar, 1000 Å. The insets in each case are enlarged areas (bar, 500 Å) and their computed difractograms where the spacing of the main equatorial spots is indicated.

Figure S10. Cryo-EM of BsFtsZ C-terminal constructs polymers. Related to main text. BsFtsZ-CTLA50 (**A** and **B**), BsFtsZ-CTLA100 (**C** and **D**), BsFtsZ-CTLA249 (**E** and **F**) are described in main text. Each BsFtsZ construct (50 μM) was assembled in Tris50 buffer with 10 mM $MgCl_2$ and 0.1 mM GMPCPP at 25 ºC, in the absence (**A**, **C**, **E**) or presence of 20 μM PC190723 (**B**, **D**, **F**), and polymers formed were visualized by cryo-EM. Bar, 1000 Å. The insets in each case are enlarged areas (bar, 500 Å) and their computed difractograms where the spacing of the main equatorial spots is indicated. A linear correlation of the spacing between protofilaments and the C-terminal length (excluding BsFtsZ-CTLA249) in the absence (**G**) and presence of PC190723 (**H**) resulted in 0.31 ± 0.02 Å and 0.38 ± 0.05 Å per residue, respectively.

Figure S11. Electron micrographs of negatively stained EcFtsZ polymers with GMPCPP. Related to Figure 5. EcFtsZ (4 μM except where indicated) was polymerized in Pipes250 buffer with 10 mM $MgCl_2$ and 50 μM GMPCPP at 25 °C. The assembly reaction was monitored by light scattering and samples were taken at different stages of de-polymerization due to nucleotide consumption. (**A**) Initial plateau (100% light scattering). (**B**) depolymerizing sample (40% light scattering); bars (A,B), 2000 Å. (**C, D**) representative large circular structures observed at 40% light scattering; (**E**) highly curved and mini-ring like structures observed at 5% light scattering in EcFtsZ (50 μM) depolymerizing samples; bars (C,D,E), 1000 Å.

Figure S12. Mg^{2+}-induced self-association of EcFtsZ with GDP and GMPCPP analyzed with sedimentation velocity (AUC). Related to main text. Sedimentation coefficient distribution c(s) of (A) EcFtsZ in Pipes250 buffer with 1 mM GDP and 10 mM $MgCl_2$, 25 °C, at 1.4 g/L (black line, $s_{20,w}$ = 2.4, 4.2 and 5.8 S), 2 g/L (blue line, $s_{20,w}$ = 3.3, 4.9 and 6.3 S) and 4 g/L (red line, $s_{20,w}$ = 3.1, 4.6, 5.8 and 7.1 S); (B) EcFtsZ with 0.2 mM GMPCP instead of GDP, at 2 g/L (black line, $s_{20,w}$ = 3.4, 4.8 and 6.2 S), 3 g/L (blue line, $s_{20,w}$ = 3.3, 5.0 and 6.5 S) and 4 g/L (red line, $s_{20,w}$ = 2.8, 4.1, 5.4 and 6.8 S). Note that in a self-association system in rapid equilibrium, the velocity of neither the slow nor the fast peaks at a finite protein concentration represents the sedimentation of any particular species; only when the association constant and concentration are large enough, the sedimentation of the fast peak may approach that of the rings (27). First theoretical estimates for the sedimentation coefficient of mini-rings made of 16 FtsZ monomers (Figure 5H) were calculated (Methods). For a ring of 220 A diameter made of spheres equivalent to a 3.2 S monomer (Figure 1), $s^o_{20,w}$ = 15.3 S; for a model ring made of monomer core structures (Figure S2, model j), $s^o_{20,w}$ = 13 S; and from the ring average cryo-EM volume (Figure 5H), $s^o_{20,w}$ = 14 S.

Figure S1

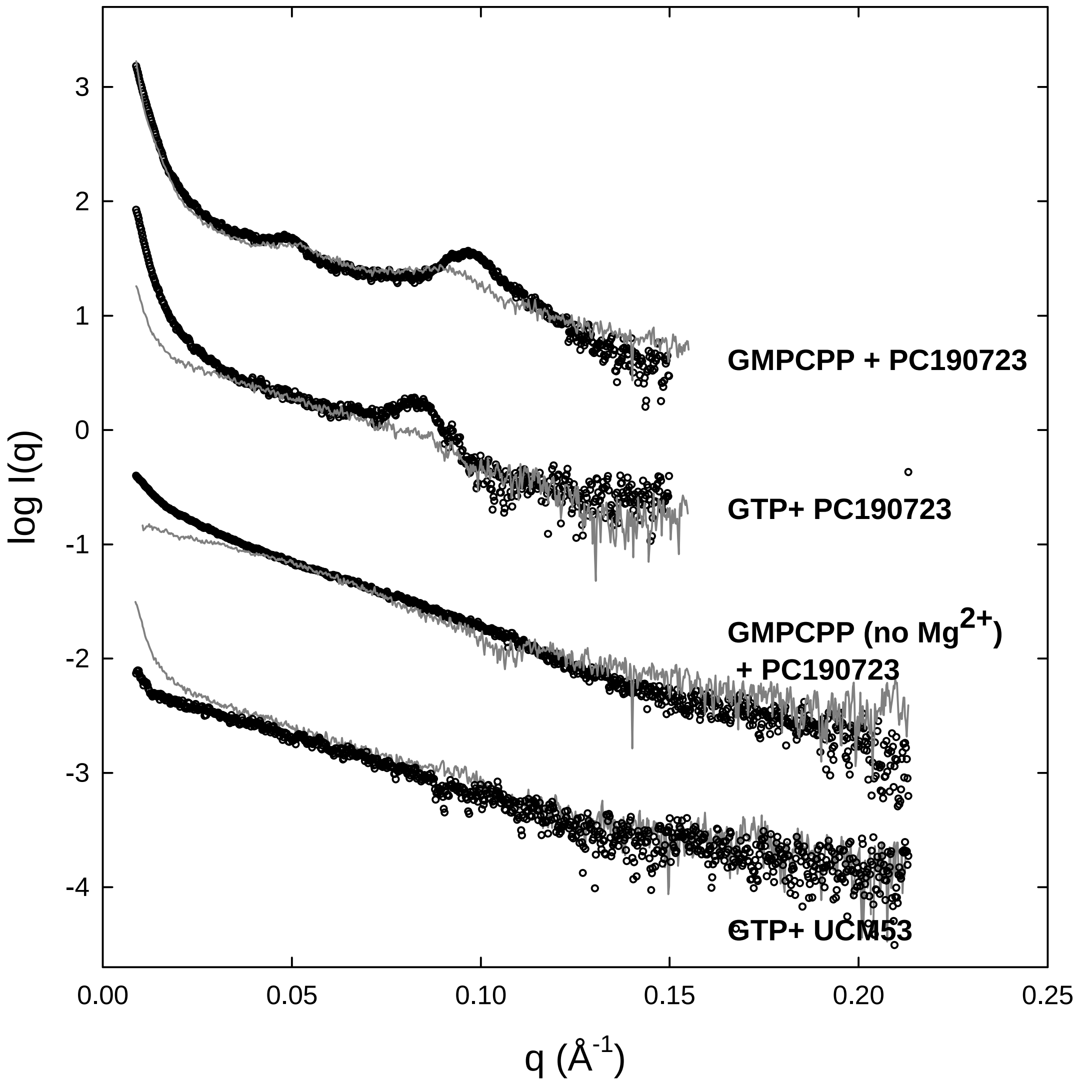

3
2
1
0
-1
-2
-3
-4
log I(q)
0.00
0.05
0.10
0.15
0.20
0.25
q (Å^{-1})
GMPCPP + PC190723
GTP+ PC190723
GMPCPP (no Mg^{2+}) + PC190723
GTP+ UCM53

Figure S2

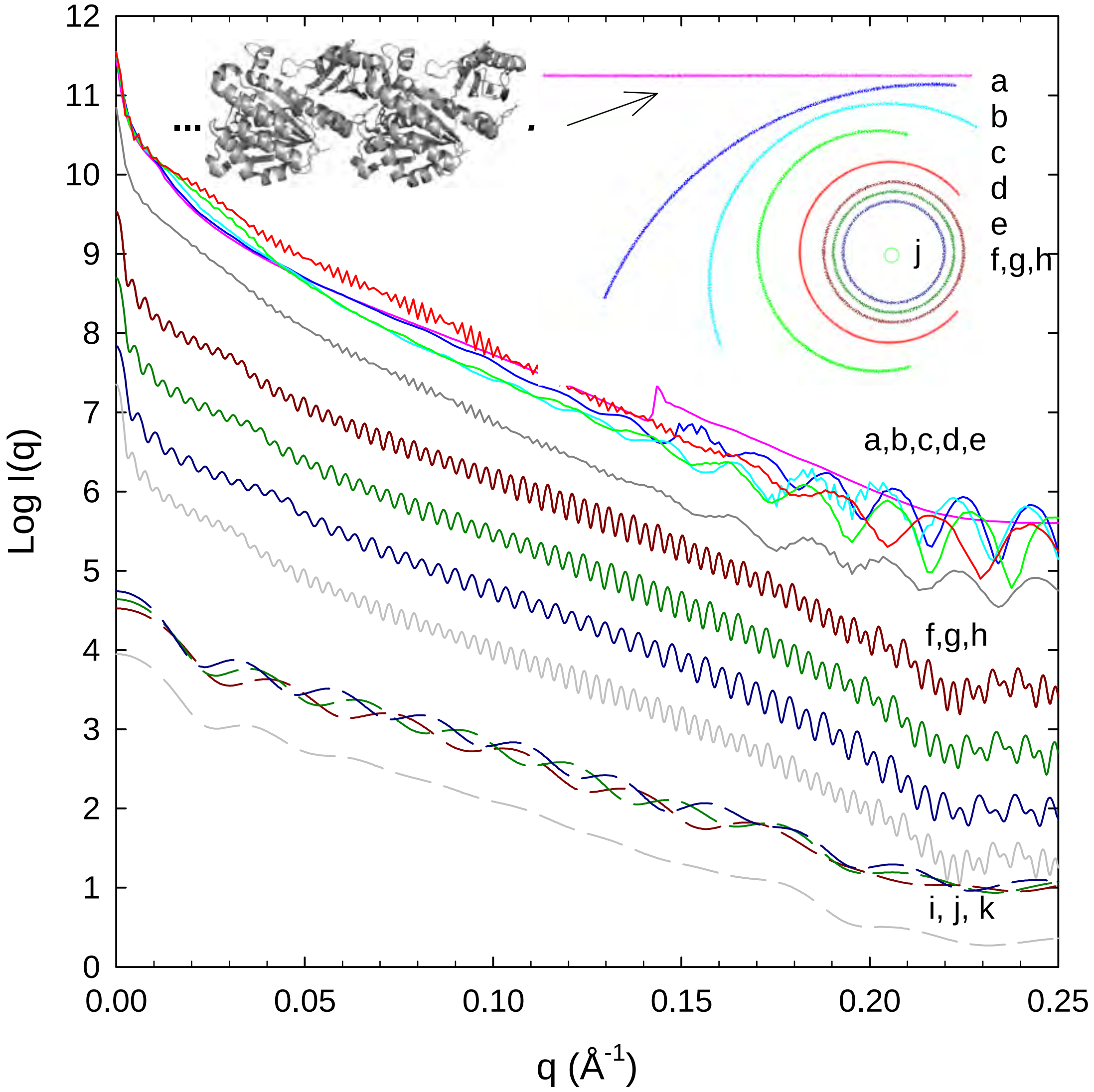
12
11
10
9
8
7
6
5
4
3
2
1
0
Log I(q)
0.00
0.05
0.10
0.15
0.20
0.25
q (Å^{-1})
...
.
a
b
c
d
e
f,g,h
j
a,b,c,d,e
f,g,h
i, j, k

Figure S3

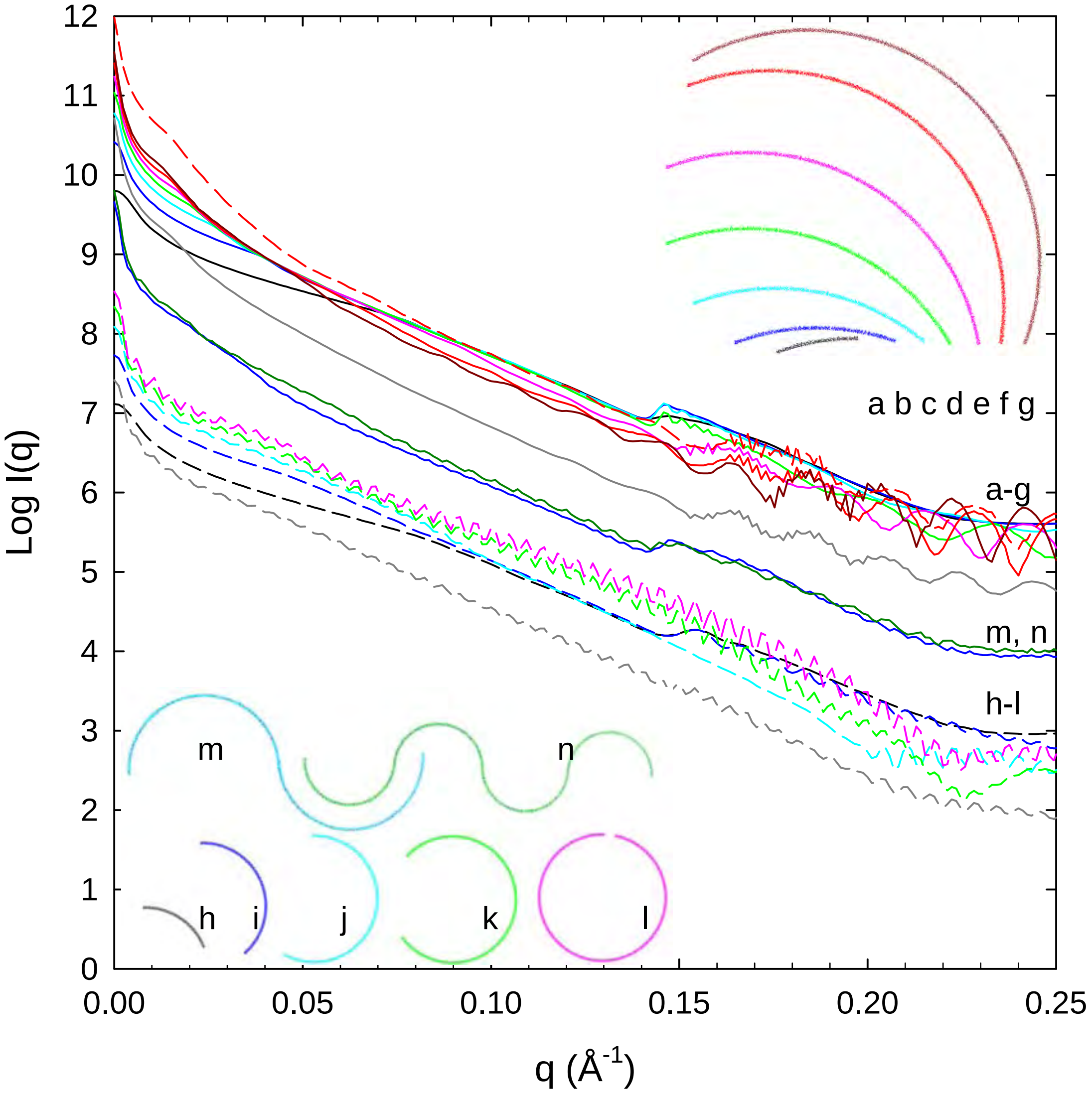
12
11
10
9
8
7
6
5
4
3
2
1
0
Log I(q)
0.00
0.05
0.10
0.15
0.20
0.25
q (Å^{-1})
a b c d e f g
a-g
m, n
h-l
m
n
h
i
j
k
l

Figure S4

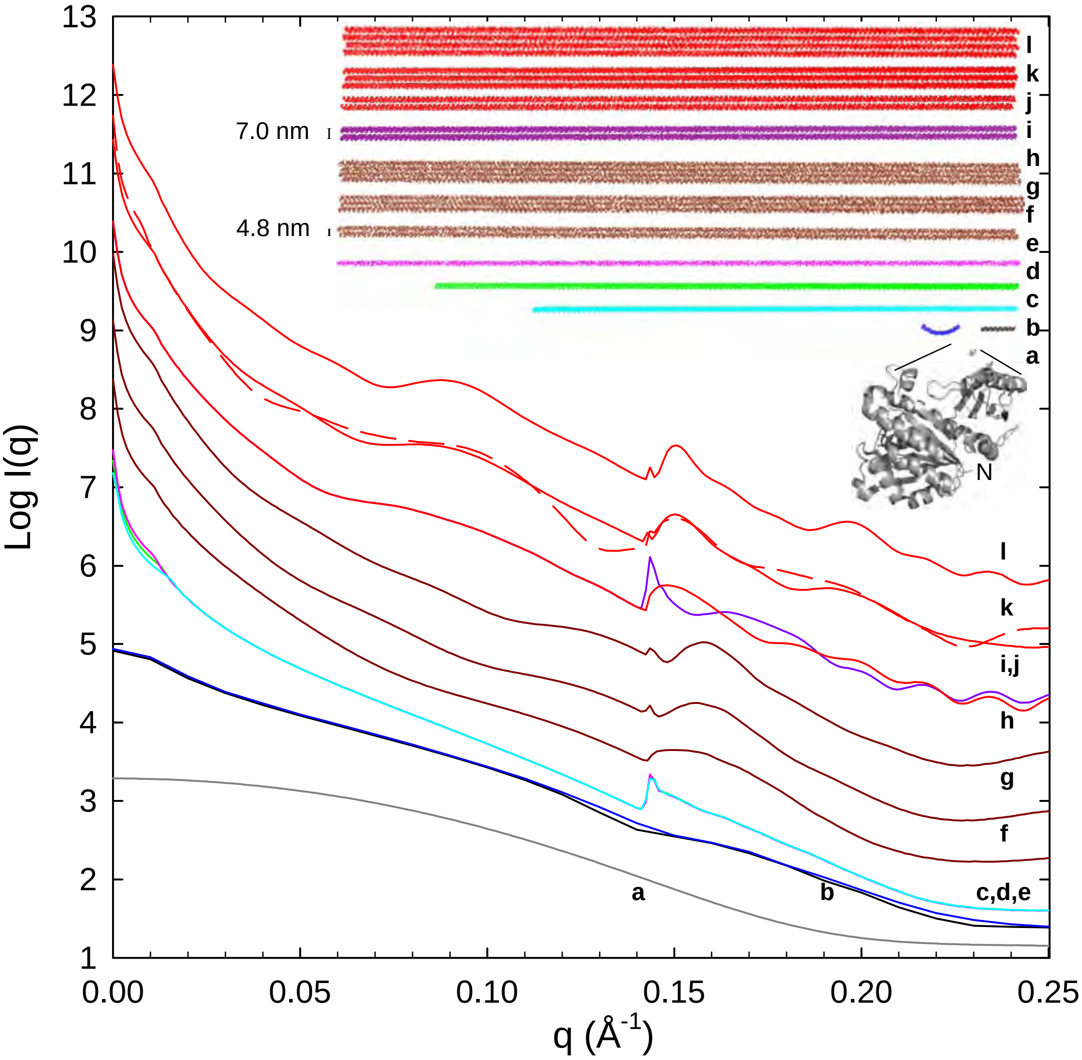

13
12
11
10
9
8
7
6
5
4
3
2
1
Log I(q)
0.00
0.05
0.10
0.15
0.20
0.25
q (Å-1)
7.0 nm
4.8 nm
l
k
j
i
h
g
f
e
d
c
b
a
N
l
k
i,j
h
g
f
a
b
c,d,e

Figure S5

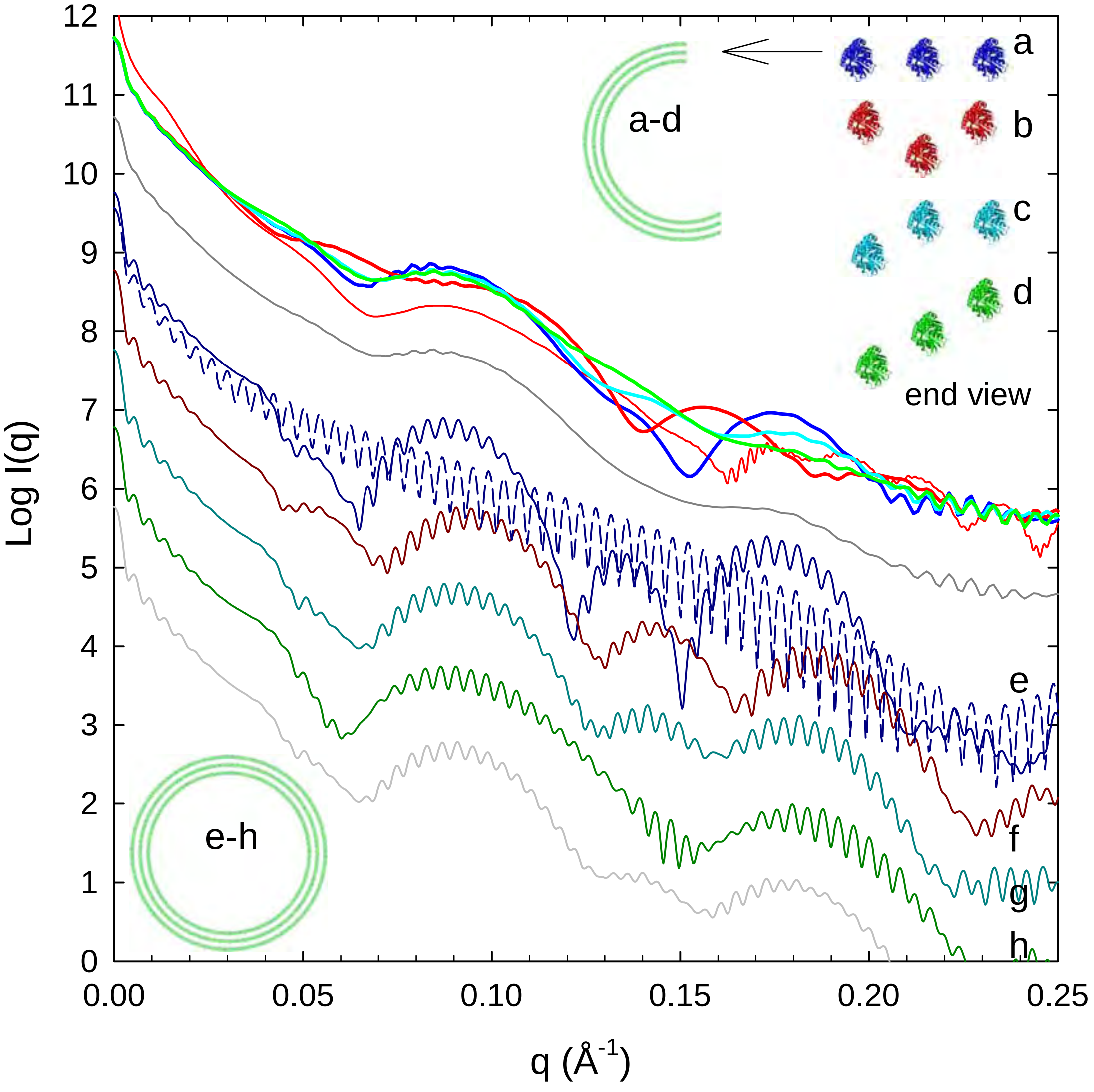

12
11
10
9
8
7
6
5
4
3
2
1
0
Log I(q)
0.00
0.05
0.10
0.15
0.20
0.25
q (Å^{-1})
a-d
a
b
c
d
end view
e
f
g
h
e-h

Figure S6

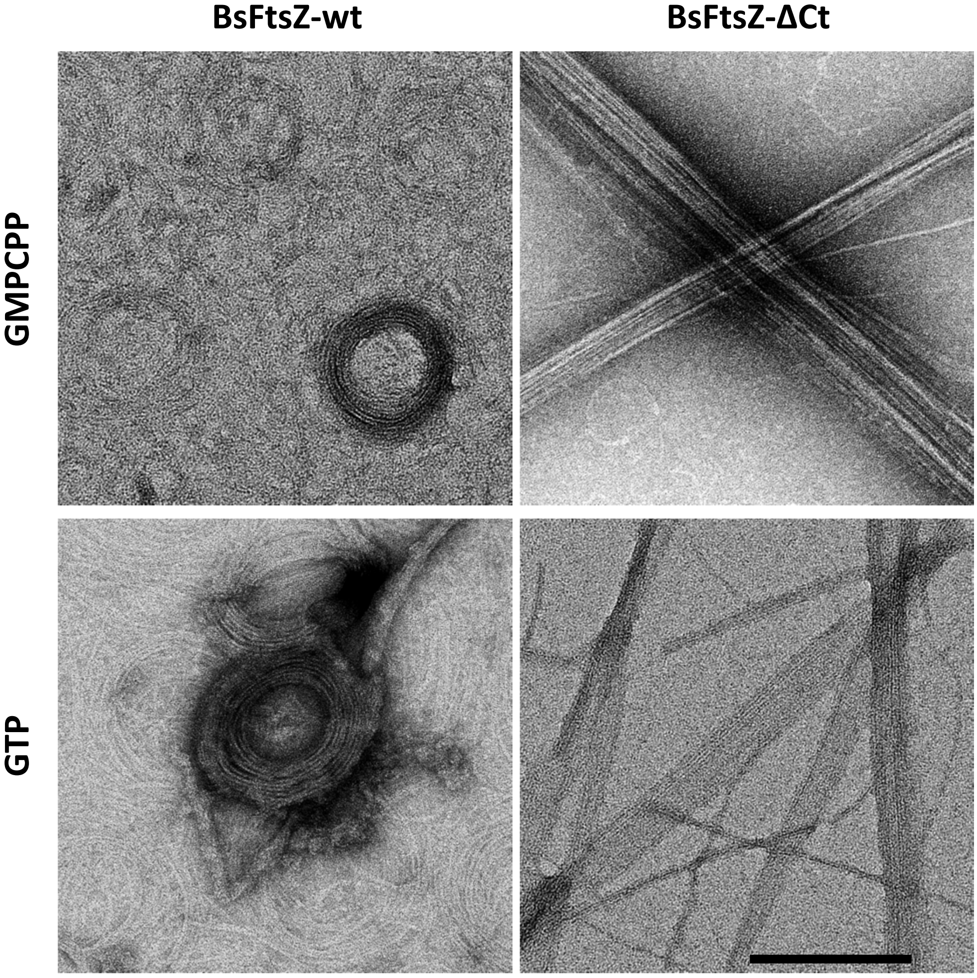

Figure S7

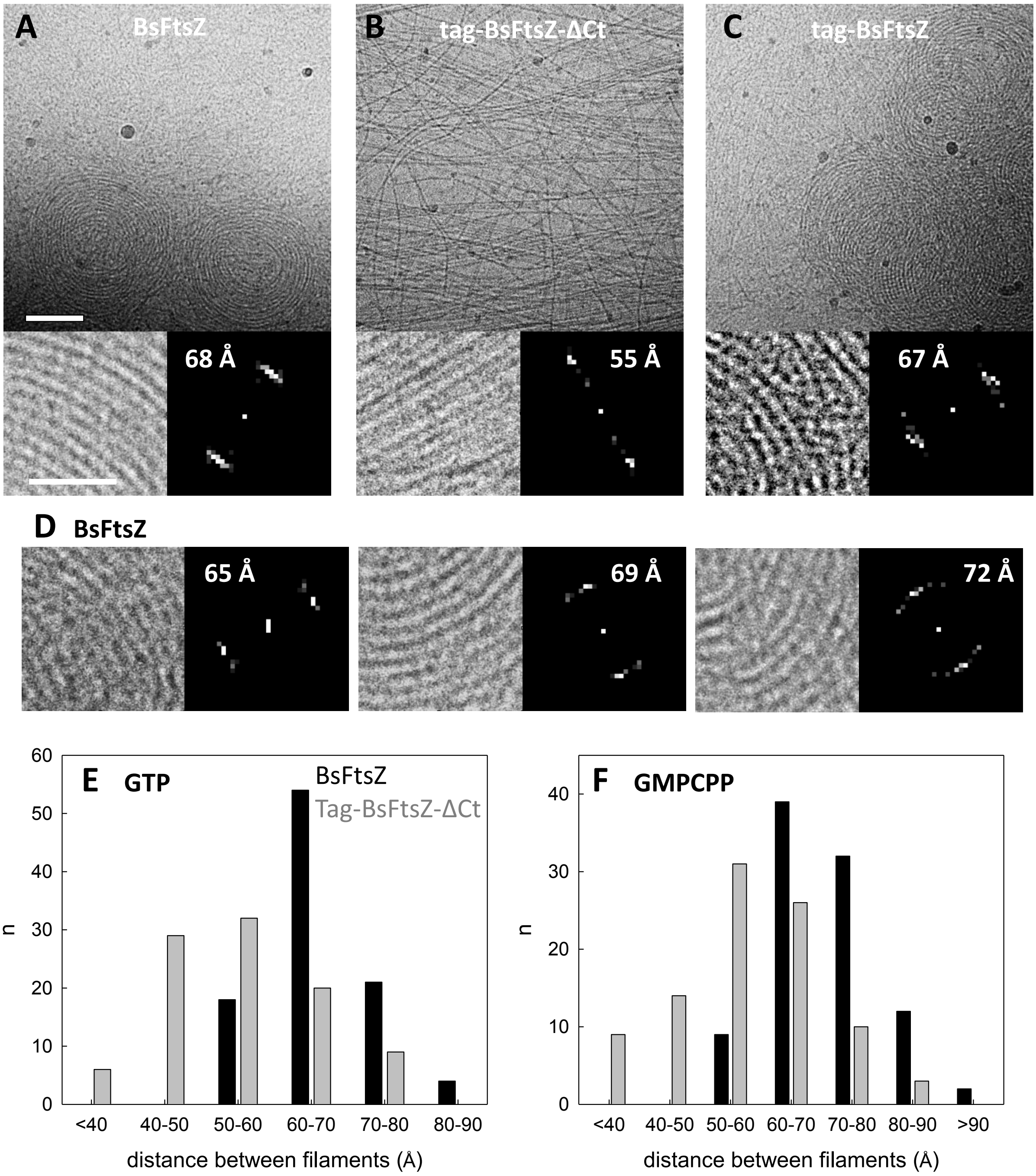
A
BsFtsZ
68 Å
B
tag-BsFtsZ-ΔCt
55 Å
C
tag-BsFtsZ
67 Å
D
BsFtsZ
65 Å
69 Å
72 Å
E
GTP
BsFtsZ
Tag-BsFtsZ-ΔCt
n
0
10
20
30
40
50
60
<40
40-50
50-60
60-70
70-80
80-90
distance between filaments (Å)
F
GMPCPP
n
0
10
20
30
40
<40
40-50
50-60
60-70
70-80
80-90
>90
distance between filaments (Å)

Figure S8

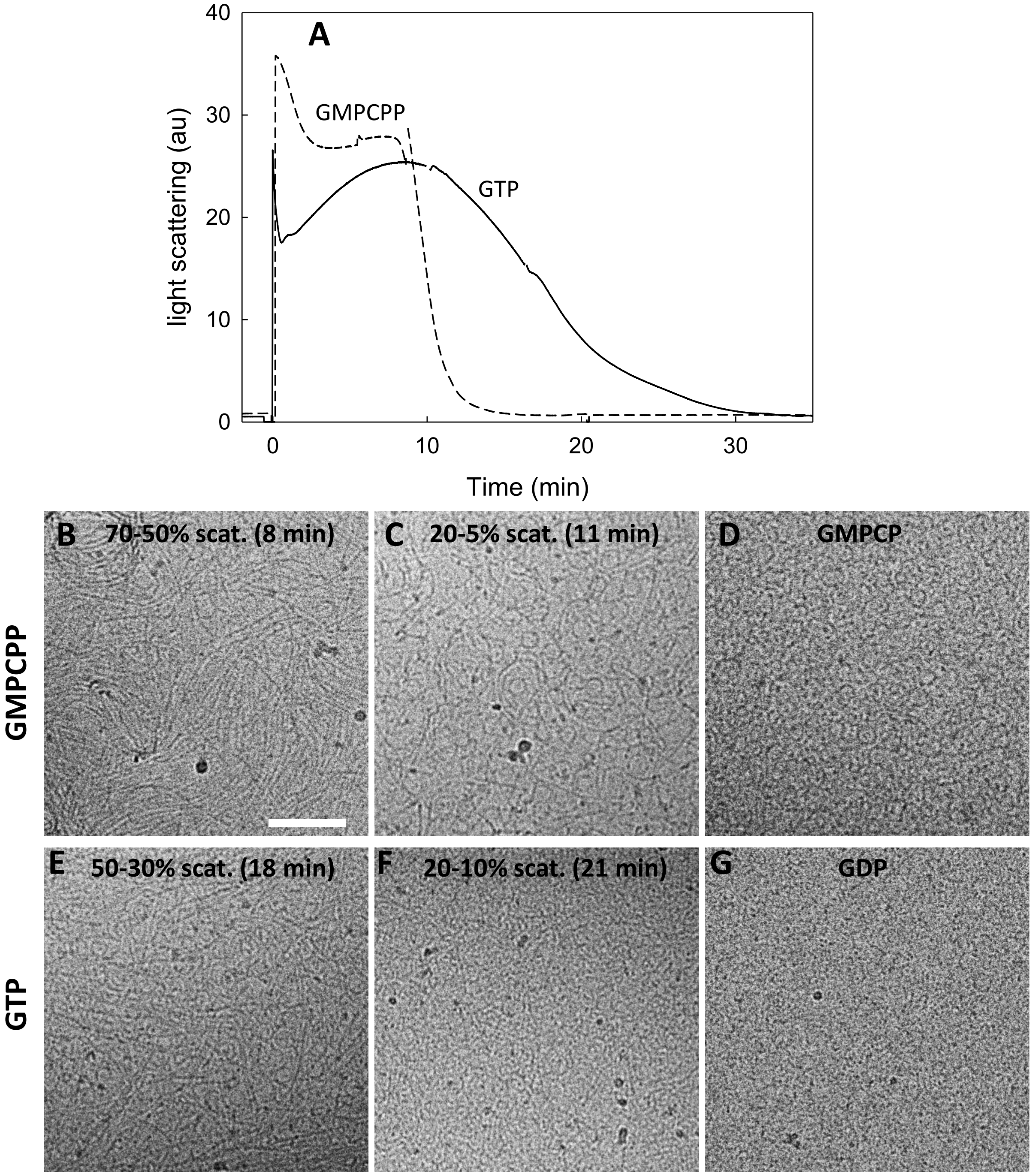
A
light scattering (au)
40
30
20
10
0
GMPCPP
GTP
0
10
20
30
Time (min)
B
70-50% scat. (8 min)
C
20-5% scat. (11 min)
D
GMPCP
GMPCPP
E
50-30% scat. (18 min)
F
20-10% scat. (21 min)
G
GDP
GTP

Figure S9

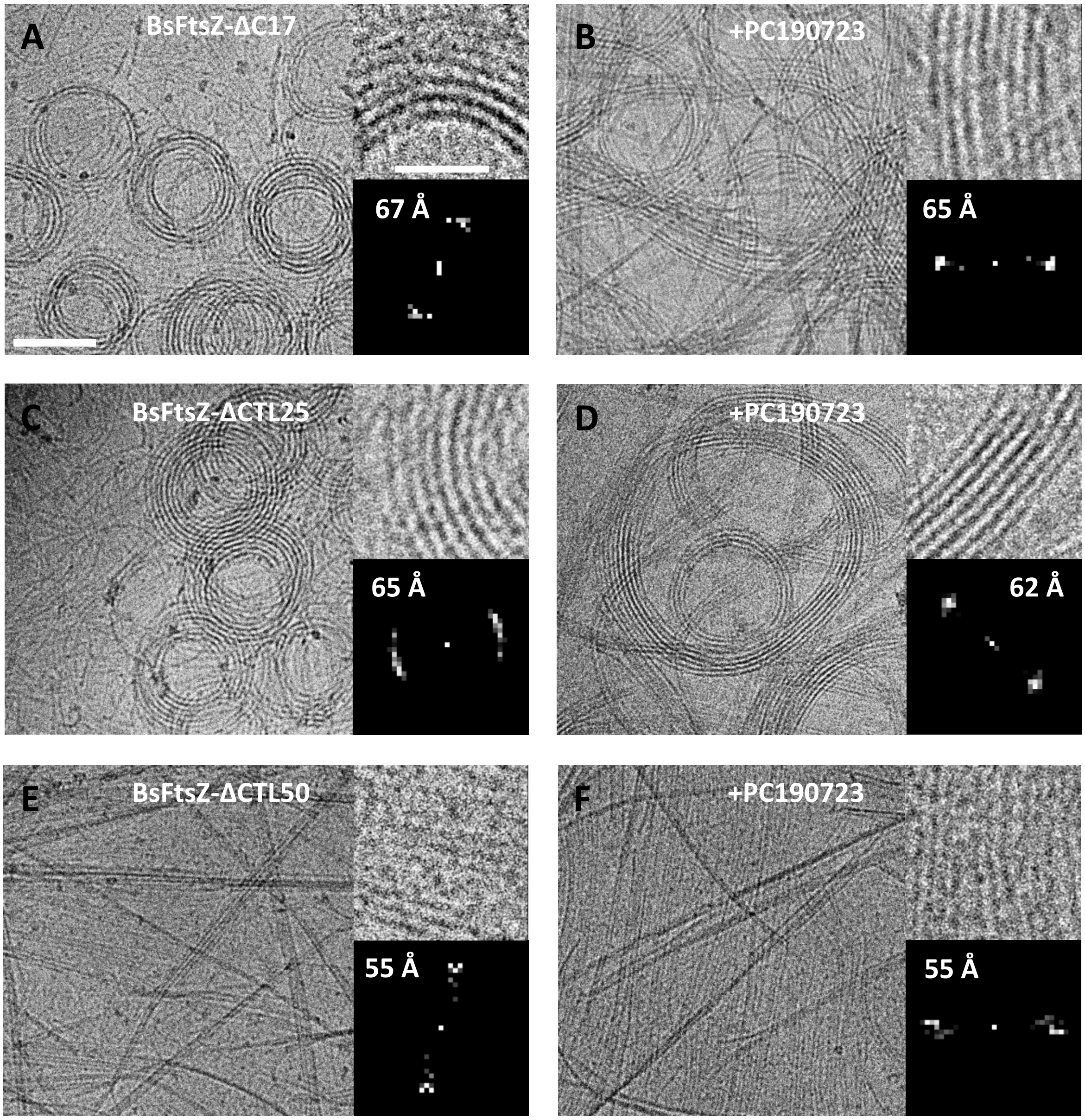
A
BsFtsZ-ΔC17
67 Å
B
+PC190723
65 Å
C
BsFtsZ-ΔCTL25
65 Å
D
+PC190723
62 Å
E
BsFtsZ-ΔCTL50
55 Å
F
+PC190723
55 Å

Figure S10

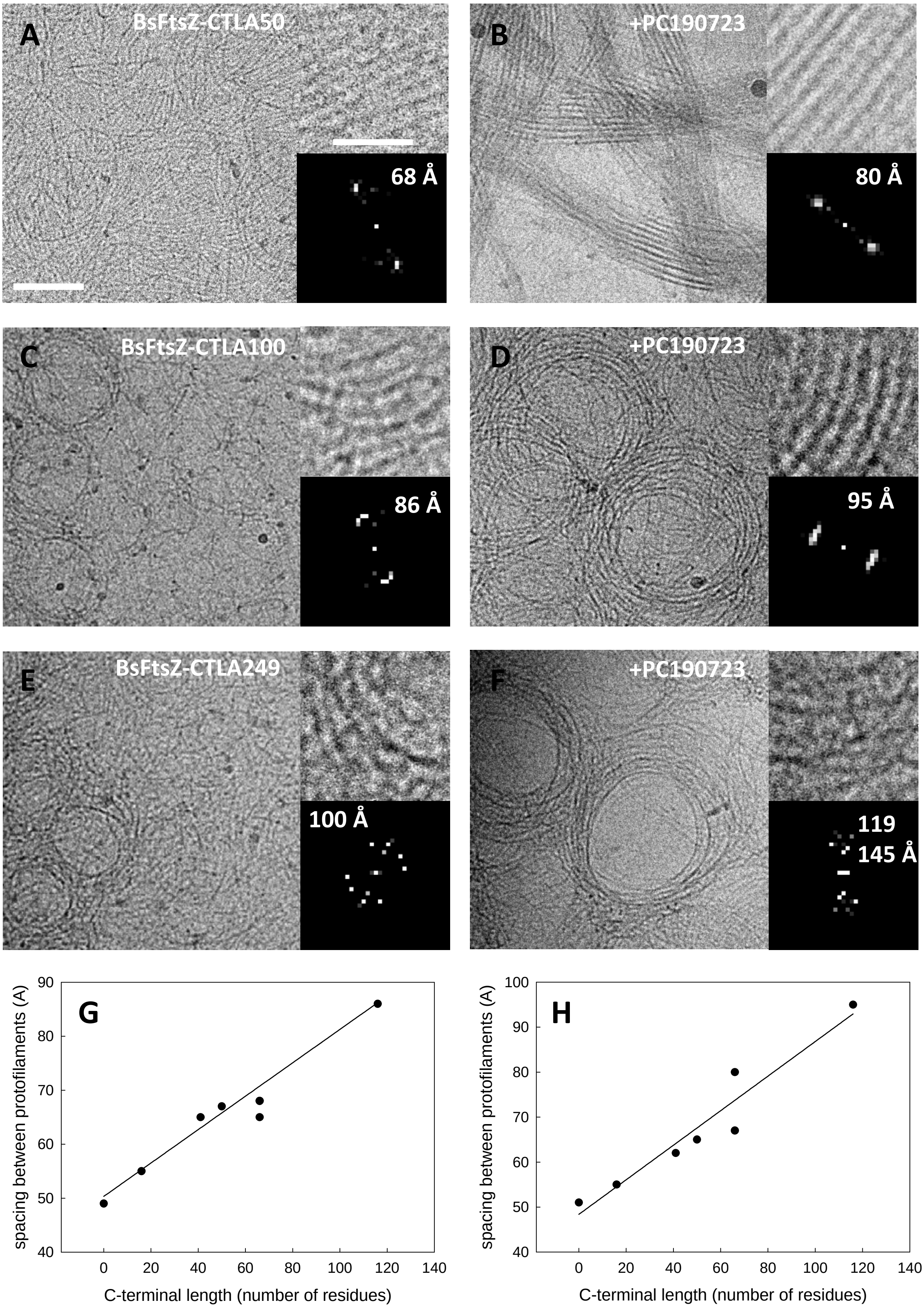
A
BsFtsZ-CTLA50
68 Å
B
+PC190723
80 Å
C
BsFtsZ-CTLA100
86 Å
D
+PC190723
95 Å
E
BsFtsZ-CTLA249
100 Å
F
+PC190723
119
145 Å
G
spacing between protofilaments (A)
90
80
70
60
50
40
0
20
40
60
80
100
120
140
C-terminal length (number of residues)
H
spacing between protofilaments (A)
100
90
80
70
60
50
40
0
20
40
60
80
100
120
140
C-terminal length (number of residues)

Figure S11

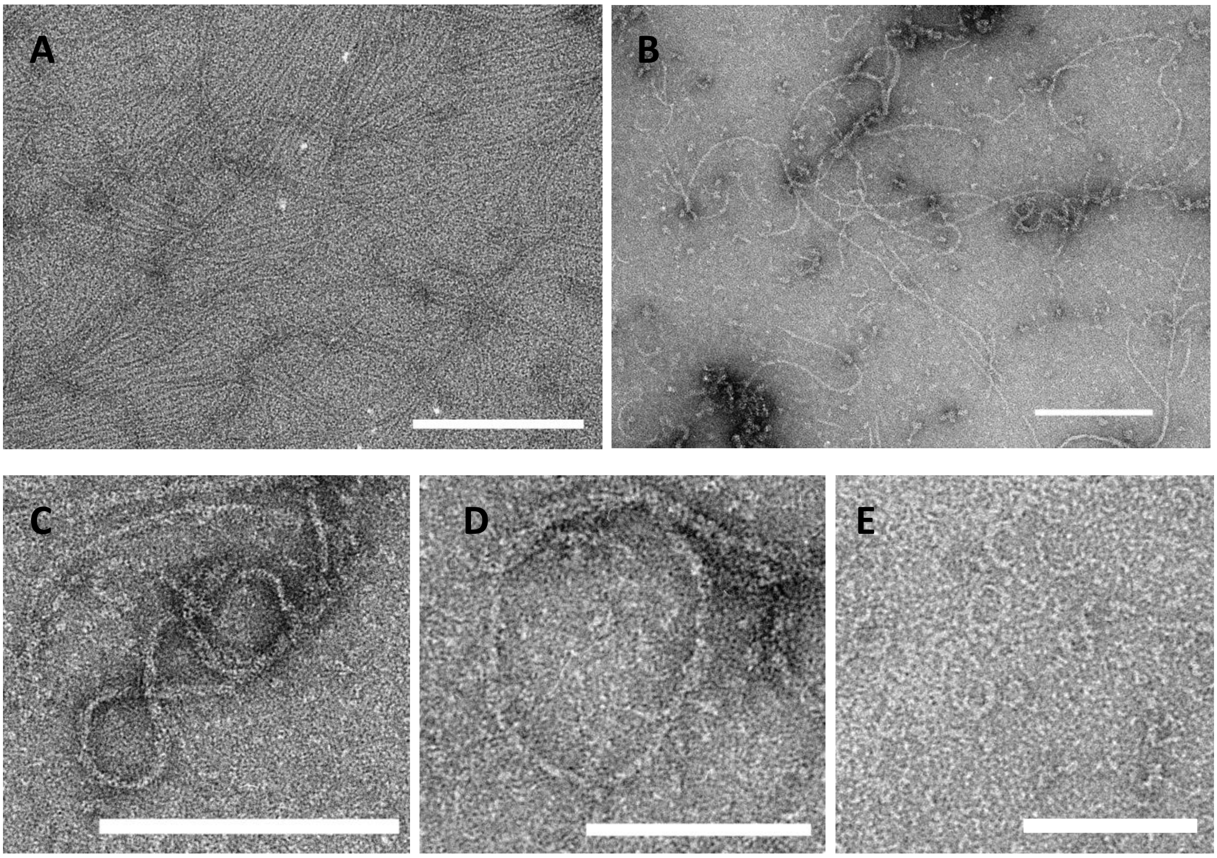

Figure S12

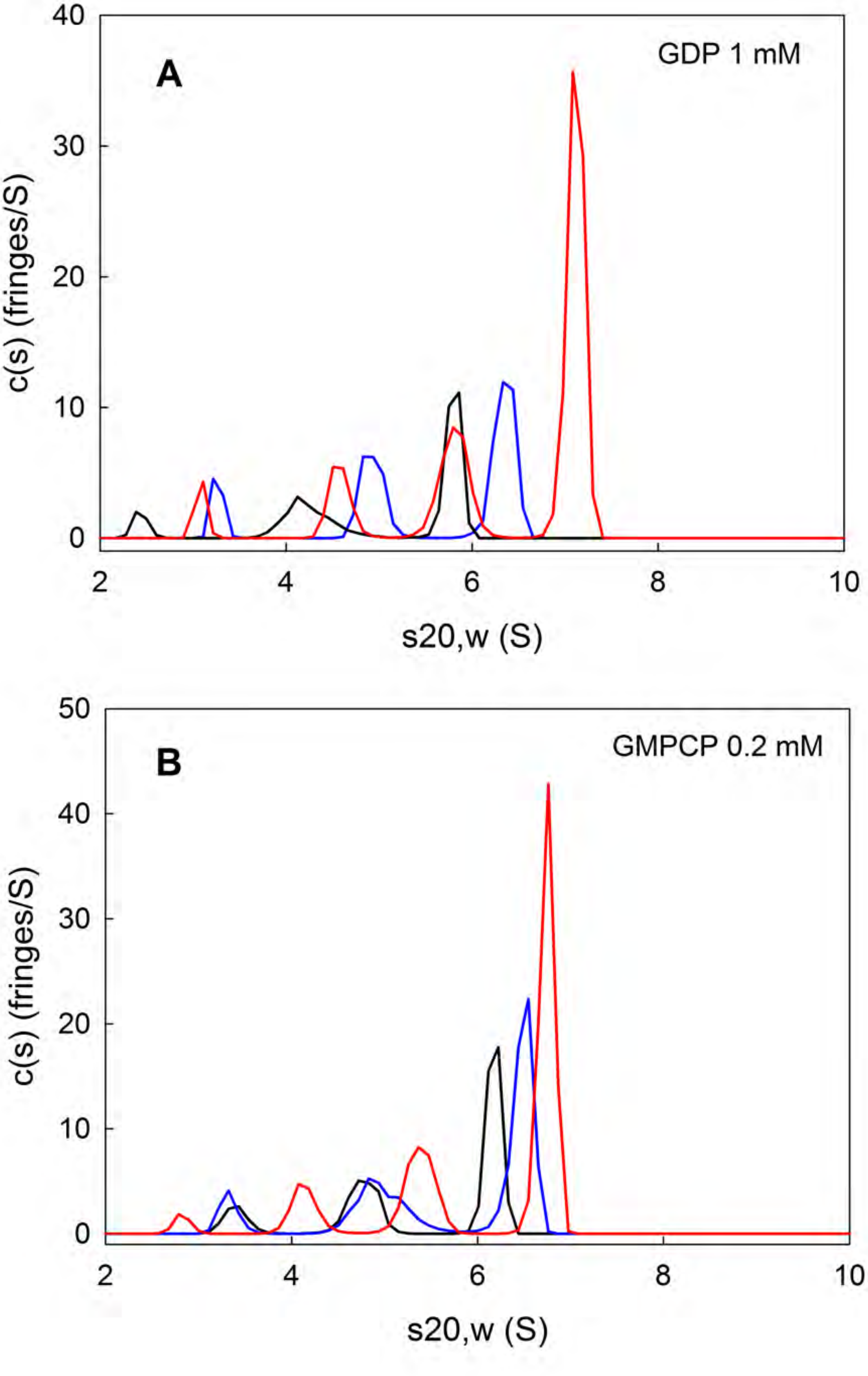
A
GDP 1 mM
c(s) (fringes/S)
40
30
20
10
0
2
4
6
8
10
s20,w (S)
B
GMPCP 0.2 mM
c(s) (fringes/S)
50
40
30
20
10
0
2
4
6
8
10
s20,w (S)